Viscoelastic fluid flow simulations in the e-VROC^{TM} geometry

Konstantinos Zografos[a,*], William Hartt[b], Mark Hamersky[b], Mónica S. N. Oliveira[c], Manuel A. Alves[d], Robert J. Poole[a]

[a] *School of Engineering, University of Liverpool, Brownlow Street, Liverpool L69 3GH, UK*
[b] *The Procter & Gamble Co., TSDC 2N-09B, 5280 Vine Street, Cincinnati, OH 45217*
[c] *James Weir Fluids Laboratory, Department of Mechanical and Aerospace Engineering, University of Strathclyde, Glasgow G1 1XJ, UK*
[d] *Centro de Estudos de Fenómenos de Transporte, Departamento de Engenharia Química, Faculdade de Engenharia da Universidade do Porto, 4200-465 Porto, Portugal*

Abstract

Microfluidic contraction devices have been proposed for extensional rheometry measurements, in particular as a useful method for determining the extensional viscosity of low elasticity solutions. The first commercially available "Extensional Viscometer-Rheometer-On-a-Chip" (e-VROC^{TM}), developed by Rheosense, is a hyperbolically-shaped contraction/expansion geometry which incorporates pressure-drop measurement capabilities. To better understand the underlying flow kinematics within this geometry we have conducted a numerical study performing three-dimensional numerical simulations for both Newtonian and viscoelastic fluids. For the viscoelastic fluids the simplified Phan-Thien and Tanner (sPTT) and the Finitely Extensible Nonlinear Elastic models (FENE-P) are employed, in order to investigate the efficiency of this configuration in terms of increasing Weissenberg numbers and to understand the effects of various model parameters on the flow field. Our Newtonian fluid results suggest that the e-VROC^{TM} geometry produces only a small region of extensional flow and is mainly shear-dominated, potentially suggesting any pressure-drop measurements from this device may be related to viscoelastic first normal-stress differences developed via a combination of shear and extension, rather than solely pure extension. By a careful selection of the sPTT and FENE-P model parameters, such that steady-state viscometric properties in homogeneous flows are matched, we are able to show that a small enhanced pressure-drop is seen for both models, which is larger for the FENE-P model.

Keywords: Extensional flow, converging/diverging channels, Viscoelastic fluids, Rheometer-on-a-chip, sPTT, FENE-P

1. Introduction

Extensional flows are observed in the majority of physical fluid flows that occur around objects or inside ducts, due to the generation of streamwise velocity gradients [1]. Such ubiquity is therefore of great importance for a large number of industrial and scientific applications which deal with fluids that are characterised by a complex microstructure (synthetic polymers, biofluids) or other types of strain-sensitive materials (e.g. droplets, cells). It is well known that in an extensional flow of either Newtonian or non-Newtonian fluids, the extensional viscosity measuring the extensional resistance of the fluid to the applied stretching rate may be significantly different from its shear viscosity. In particular for a Newtonian fluid, the ratio between the extensional viscosity and the shear viscosity is three for uniaxial flow and four in planar flows [2]. On the contrary, when a critical extension rate is achieved for viscoelastic fluids, the extensional resistance of the fluid flow can dramatically increase compared to the equivalent shear resistance, with this difference depending on the deformation and deformation rate [2–4]. Therefore, the extensional properties of the fluid may significantly affect its flow, and need to be taken into account when designing devices to manipulate the fluid of interest. Characterising the extensional properties of various biofluids, such as blood, plasma, saliva, synovial fluid, is also of great importance from a therapeutic and/or a diagnostic point of view. It is known that large deviations from their normal values can be associated directly with serious diseases or organ dysfunctions [5]. For example, measuring and understanding the deformability of red blood cells can provide valuable information in order to detect several diseases such as diabetes or malaria [6, 7]. Additionally, understanding the rheological properties of a variety of commercial/synthetic fluids, from processed food-products up to cosmetics and liquid detergents, helps to achieve a certain final quality of the desired product [8, 9]. There is a clear need for appropriate tools that can produce well-defined flow fields in order to provide scientists with the ability to measure accurately the extensional properties of the fluids of interest. Although this has been long discussed and several designs have been reported, we believe that there is still room left for more efficient designs and methods.

Lab-on-a-chip devices have been recognised for their potential to provide meaningful measurements in the context of rheological studies [1, 10]. The operational small length scales (1 μm - 1000 μm) of microfluidic devices offer the ability to generate large deformations and deformation rates for typically low flow rates. In this way, the relevant mechanical proper-

*Corresponding author
Email address: k.zografos@liv.ac.uk (Konstantinos Zografos)

ties of the fluids of interest are enhanced, compared to macro-scale flows where they are usually masked by inertial effects [4]. Moreover, in scientific fields that are related to biomedical research the samples used may be very expensive or impossible to produce in larger volumes. Thus, the small amounts that are needed in order to perform experiments in micro-configurations (and consequently the low amount of the final waste), together with their potential for portability and their ability to reproduce controlled, three-dimensional environments, increased their potential and made them a promising candidate over other conventional techniques [10, 11]. Focusing on the rheological behaviour and the characteristics of complex fluids, microfluidic technology, as highlighted by Pipe and McKinley [12] for example, offers advantages towards their investigation and characterisation, both under shear and extensional deformation. Configurations for evaluating the fluid's shear viscosity of complex fluids have been very successful and several techniques have been reported in the reviews of Pipe and McKinley [12] and Sousa *et al.* [10]. On the other hand, accurate measurement of the extensional viscosity is arguably a very difficult task with limited practical success achieved to date [1]. Several microfabricated configurations appropriate to the characterisation of extensional flows of complex fluids, have been reported in the recent reviews by Galindo-Rosales *et al.* [13] and Haward [1]. The majority of these configurations follow the key idea used in shear viscometers, that is to measure shear viscosity in well-controlled conditions where the flow is viscometric. Thus, in a similar way, these extensional flow devices aim to generate flow conditions where the extension rate is constant in both space and time in order to allow for accurate measurements of the steady-state extensional viscosity.

Internal flow configurations able to generate the appropriate flow conditions for extensional flows are briefly distinguished in three categories: those which exploit their geometrical characteristics in order to stretch the fluid that flows within (e.g. contraction flows); those that are able to manipulate multiple streams generating stagnation point flows (e.g. cross-slot, T-junction); those that consider flows of multiple fluid streams and produce a stretching flow that is applied on the desired sample (e.g. flow-focusing).

In this paper we focus on the first category of designs, which is arguably the most frequently used in studies related to extensional flows. Contraction or contraction/expansion geometries can either be abrupt or smooth, and have been extensively used experimentally for investigating the mechanisms of fluid elasticity [14–18]. Abrupt contractions, in particular, have been recognised as probably the most suitable geometries for benchmarking the efficiency of computational methods that are related to non-Newtonian fluids [19–22]. The simplicity of these type of designs, both in terms of manufacturing and fluid handling (only one fluid stream needs to be controlled), is an important advantage over the other methods discussed above. At the same time, they are able to generate flows that are characterised by a combination of strong shear effects close to the walls and strong extension in the vicinity of the contraction [23, 24]. This characteristic was further exploited numerically by using either contraction, expansions or contraction/expansion geometries, for assessing the effects of elasticity in flows of viscoelastic fluids [18, 23, 25–29]. Considering the general case of the abrupt contraction/expansion, the basic drawback of this design is that the extension generated is non-homogeneous, because of entrance and exit effects near the vicinity of the contraction/expansion region and only exposing the fluid to finite strains which are determined by the contraction ratio (a true steady-state extensional flow corresponding to infinite strain is therefore potentially not obtainable). Thus, this configuration is unlikely to establish a considerable region of constant strain-rate, making abrupt constrictions unsuitable candidates for extensional rheometry [16, 17]. On the other hand, smooth contraction/expansion geometries are expected to produce more uniform extension rates [30, 31]. The significance and the importance of constrained converging flows were originally presented by Cogswell [30, 32], demonstrating how elongation can be enforced and therefore, how these flows can assist in extensional flow rheological measurements. More specifically, it was discussed that when a fluid is flowing within a die, the average velocity will gradually increase along the flow direction due to the progressive increase of the constriction. Thus, a constant, maximum, stretch rate that occurs along the centreline of the flow will result. Later, the principles of a hyperbolic converging rheometer were introduced by James *et al.* [31], where the advantages of this type of geometry to operate as extensional rheometers have been demonstrated. It was argued that a hyperbolically-shaped geometry can be employed in order to apply constant strain-rates to a desired sample or a fluid element that flows along the centreline of the flow. Oliveira *et al.* [18] were motivated by this and considered a microfluidic channel that was designed with a hyperbolic contraction that was followed by an abrupt expansion. The authors investigated the performance of this device as a potential microfluidic rheometer both numerically and experimentally considering Newtonian fluids only. The flow however was found to be non-homogeneous where the developed strain-rate deviated from the "ideal" uniform strain-rate profile. Ober *et al.* [24], extended the study and considered a symmetric hyperbolic contraction/expansion designed with the same hyperbolic function and introduced the "Extensional Viscometer-Rheometer-On-a-Chip" (e-VROC^{TM}) geometry. The authors stated that their design was capable of indexing and comparing the flow of several complex fluids up to a specific value of extension rates, by performing detailed pressure-drop measurements along the contraction/expansion. However, similar to Oliveira *et al.* [18], the authors reported that entrance and exit effects occur in a region with non-homogeneous flow that has combined shear and elongational characteristics. Later, Keshavarz and McKinley [33] reported that the e-VROC^{TM} geometry will not perform efficiently for low viscosity dilute polymer solutions, since the hyperbolic contraction/expansion is affected by non-linear inertial effects. In the same study, the authors proposed the "Rayleigh Ohnesorge Jetting Extensional Rheometry" (ROJER) as an alternative technique.

Configurations especially designed with a smooth constriction have found so far a number of applications. McKinley *et al.* [27] employed a hyperbolic contraction geometry for esti-

mating the apparent extensional viscosity of polyethylene oxide solution. Similar designs were used for investigating the flow of low viscosity Boger fluids [34] and also for mimicking flows along stenoses in the human micro-circulatory system using blood analogue solutions [35]. Additionally, they have been employed to study the deformability of white blood cells [36] and that of red blood cells under strong extensional flow, and have been recognised for their potential use in diagnosis of blood diseases [7, 37, 38]. Furthermore, smooth converging/diverging geometries are employed for modeling and investigating the dynamics of drop deformation [39, 40]. Recently, a series of optimised converging/diverging designs have been proposed by Zografos *et al.* [41], which are able to generate well-defined and controlled flow kinematics. The authors demonstrated that the efficiency of the hyperbolic design will depend on the length of the contraction, but they also illustrated, that depending on the depth of the microfluidic channel, different optimised shapes able to generate controlled extensional flow exist. Lee and Muller [42] proposed a method for generating fully-developed elongational flow at a nearly constant extension rate within a converging microchannel and proposed a "differential pressure extensional rheometer on a chip".

In this work, we investigate using numerical simulations the performance of the "Extensional Viscometer-Rheometer-On-a-Chip" (e-VROC^{TM}) proposed by Ober *et al.* [24], considering both Newtonian and viscoelastic fluids. The remainder of the paper is organised as follows: Initially, in Section 2 the geometrical characteristics of the e-VROC^{TM} configuration are presented, together with the desired behaviour that a design of this type should ideally produce, in order to achieve a region of constant strain-rate. Section 3 presents the equations of motion together with the characteristic dimensionless numbers of the flow and the viscometric properties of the viscoelastic models employed. In Section 4, the performance of the e-VROC^{TM} is discussed by presenting the results obtained from the computational fluid dynamics (CFD) simulations for Newtonian and viscoelastic fluids while finally, in Section 5, the main conclusions of the study are outlined.

2. Configuration of e-VROC^{TM}

The geometrical characteristics of the e-VROC^{TM} geometry first proposed by Ober *et al.* [24] are shown schematically in Fig. 1. The geometry is defined by the upstream width $w_1 = 2H_1 = 2920\,\mu$m, the contraction width $w_2 = 2H_2 = 400\,\mu$m, the contraction length $l_c = 400\,\mu$m (cf. Fig. 1a) and the nominal depth of the channel $d = 200\,\mu$m (cf. Fig. 1b). The dimensions of the geometry result in an upstream aspect ratio AR $= w_1/d = 14.6$ and in a contraction ratio CR $= w_1/w_2 = 7.3$, which gives a Hencky strain $\epsilon_H \approx ln(\text{CR}) \approx 2$. It should be highlighted that along the constriction the channel aspect ratio varies, reaching to its minimum value, AR $= 2$, exactly at the throat of the converging/diverging contraction. Based on these geometrical characteristics, Ober *et al.* [24] were able to design the shape of the hyperbolic boundaries of the symmetric converging/diverging constriction as is shown in Fig. 1a, using a hyperbolic function similar to that first employed by Oliveira *et al.* [18]. The boxes included in Fig. 1a demonstrate schematically the original locations of the four pressure sensors in the e-VROC^{TM} microfluidic chip, which are responsible for measuring the pressure-drop along the constriction. From the pressure sensors the authors were able to collect pressure data and evaluate the pressure-drop: (i) in the fully-developed region upstream of the contraction region, ΔP_{12} using sensors 1 and 2; (ii) in the fully-developed region downstream of the constriction, ΔP_{34} using sensors 3 and 4; (iii) across the constriction, ΔP_{23} using sensors 2 and 3. Pressure sensors 2 and 3 are located at a certain distance upstream of the start of the contraction and downstream of the end of the expansion and thus, Ober *et al.* [24] introduced Eq. (1) for evaluating the pressure-drop along the contraction/expansion, which attempts to remove the influence of this extra distance:

$$\Delta P_c = \Delta P_{23}\left[1 - \frac{1}{2}\left(\frac{1}{\mathcal{P}} - 1\right)\frac{L_{23} - 2l_c}{L}\right]. \tag{1}$$

The pressure coefficient $\mathcal{P}$ is defined as $\mathcal{P} = \Delta P_{23}/\Delta P_{14}$ and $L = L_{12} = L_{34}$, with the notation L_{ij} indicating the distance between pressure sensors i and j. After obtaining the pressure-drop measurements, Ober *et al.* [24] were able to estimate the excess pressure-drop along the contraction/expansion due to elastic normal stresses, $\Delta P_{c,e}$, by subtracting the viscous contributions to the pressure-drop, $\Delta P_{c,v}$, from the estimated pressure-drop along the constriction:

$$\Delta P_{c,e} = \Delta P_c - \Delta P_{c,v}. \tag{2}$$

Having evaluated the excess pressure-drop along the constriction, they were finally able to estimate the extensional viscosity of the examined fluids. Ober *et al.* [24] proposed that the first normal-stress difference can be approximated by $N_1 = \Delta P_{c,e}/\epsilon_H$, and combined it with the material function for the

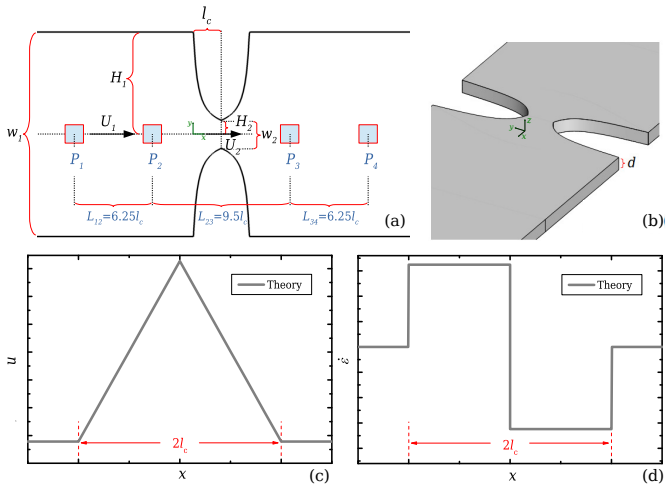

Figure 1: e-VROC^{TM} configuration with $w_1 = 2H_1 = 2920\,\mu$m, $w_2 = 2H_2 = 400\,\mu$m, $l_c = 400\,\mu$m, $d = 200\,\mu$m. (a) Bird's-eye view where the boxes illustrate schematically the location of the pressure sensors (cf. [24]); distances are not to scale. Isometric view (b) and ideal velocity (c) with the normalised strain-rate (d) profiles along the centreline of the flow in a hyperbolic-shaped geometry assuming that the flow is fully-developed everywhere.

extensional viscosity, $\eta_e = N_1/\dot{\epsilon}$, where $\dot{\epsilon}$ is the applied strain-rate, to estimate η_e:

$$\eta_e = \frac{1}{\epsilon_H}\frac{\Delta P_{c,e}}{\dot{\epsilon}}. \tag{3}$$

Figure 1 also shows the ideal performance of a geometry designed to operate as an extensional rheometer. More specifically, as shown in Fig. 1c the ideal velocity profile, u, along the flow centreline is expected to vary linearly to provide regions of homogeneous extension, and preferably a geometry that is designed to perform measurements of the extensional properties of fluids should approximate it [41, 43]. Considering a fluid element which travels along the flow centreline, the strain-rate experienced is expressed by the velocity gradient along the streamwise direction, $\dot{\epsilon} = \partial u/\partial x$. This particular ideal velocity profile, yields the ideal constant strain-rate profile illustrated in Fig. 1d, resulting in a homogeneous extension along the flow centreline with a positive value in the converging part and a negative value in the diverging part. This apparent constant value is then used in conjunction with Eq. (3) to provide an estimate of η_e.

It should be mentioned here that the viscous contributions needed in Eq. (2) were evaluated in Ober *et al.* [24] by assuming a lubrication approximation. However, as the authors demonstrated in their study, the lubrication approximation underestimates the measured experimental values. Similarly, Lee and Muller [42] showed in their numerical study for a differential pressure extensional rheometer, that as the contraction ratio of the design increases, the lubrication approximation underestimates even more the evaluated pressure-drop. Obtaining the viscous pressure-drop along the contraction/expansion experimentally is not an easy task and thus, Lee and Muller [42] proposed an alternative microfluidic chip. Their configuration incorporates a contraction/expansion channel and a reference straight channel. The latter is designed long enough in order to generate the same pressure-drop as in the converging region, assisting to overcome this experimental difficulty and to obtain an estimate of the viscous pressure-drop. It should also be stated that the analysis above assumes a "steady-state" extensional response whereas a fluid element flowing along the centreline will experience only a finite strain, thus such a steady-state (Hencky strain approaching infinity) is not guaranteed.

3. Governing equations

The CFD simulations consider incompressible and isothermal fluid flow. Therefore, the continuity and the momentum equations are employed and solved numerically:

$$\nabla \cdot \boldsymbol{u} = 0 \quad , \tag{4}$$

$$\rho\left(\frac{\partial \boldsymbol{u}}{\partial t} + \boldsymbol{u}\cdot\nabla\boldsymbol{u}\right) = -\nabla p + \nabla\cdot\boldsymbol{\tau} \quad , \tag{5}$$

where $\boldsymbol{u}$ is the velocity vector, ρ is the fluid's density, p is the pressure and $\boldsymbol{\tau}$ is the extra stress tensor. The latter is expressed as the sum of the solvent stress component, $\boldsymbol{\tau}_s$ (Newtonian part), and the polymeric stress component $\boldsymbol{\tau}_p$:

$$\boldsymbol{\tau} = \boldsymbol{\tau}_s + \boldsymbol{\tau}_p = \eta_s\dot{\boldsymbol{\gamma}} + \boldsymbol{\tau}_p \quad , \tag{6}$$

where η_s is the solvent viscosity and $\dot{\boldsymbol{\gamma}} = \nabla\boldsymbol{u} + \nabla\boldsymbol{u}^T$ is the shear-rate tensor (for Newtonian fluids $\boldsymbol{\tau}_p = \mathbf{0}$). It is common, when investigating the response of viscoelastic fluids, to employ the ratio of the solvent viscosity to the total zero shear viscosity $\eta_0 = \eta_p + \eta_s$, known as the solvent-to-total-viscosity ratio, $\beta = \eta_s/\eta_0$, where η_p is the polymeric viscosity coefficient. Here, we examine cases where the solvent-to-total-viscosity ratio is set as $\beta = 1/9$, a typical value for solutions of relatively high polymer concentrations and cases with $\beta = 0.95$ for investigating the response of more dilute polymer solutions, with Boger fluid-like behaviour [44].

The response of viscoelastic fluids in the e-VROC$^{\text{TM}}$ geometry is investigated by considering the linear form of the simplified Phan-Thien and Tanner model (sPTT) [45] and the Finitely Extensible Nonlinear Elastic model that follows the Peterlin approximation (FENE-P) [46]. Both models are expressed here in terms of the evolution of the conformation tensor, $\mathbf{A}$:

$$\overset{\triangledown}{\mathbf{A}} = \begin{cases} -\frac{f_A}{\lambda}\left(\mathbf{A}-\mathbf{I}\right), & \text{sPTT} \\ -\frac{1}{\lambda}\left(f_A\mathbf{A} - a\mathbf{I}\right), & \text{FENE-P} \end{cases} \tag{7}$$

where $\overset{\triangledown}{\mathbf{A}}$ is the upper-convected derivative of the conformation tensor, λ is the relaxation time of the polymer and $\mathbf{I}$ is the identity tensor. The function f_A appearing in Eq. (7) is for both models a function of the trace of the conformation tensor, expressed for each case as [47, 48]:

$$f_A = \begin{cases} 1 + \varepsilon(\text{Tr}\mathbf{A} - 3), & \text{sPTT} \\ L^2/(L^2 - \text{Tr}\mathbf{A}), & \text{FENE-P} \end{cases} \tag{8}$$

while the parameter a in the FENE-P model is defined as $a = L^2/(L^2-3)$. The polymeric component of the extra-stress tensor (cf. Eq. (6)), is obtained from the conformation tensor following Kramers' form:

$$\boldsymbol{\tau}_p = \begin{cases} \frac{\eta_p}{\lambda}\left(\mathbf{A}-\mathbf{I}\right), & \text{sPTT} \\ \frac{\eta_p}{\lambda}\left(f_A\mathbf{A} - a\mathbf{I}\right). & \text{FENE-P} \end{cases} \tag{9}$$

In Eq. (8), ε and L^2 parameters are both known as the extensibility parameter of the sPTT and the FENE-P models, respectively. Focusing for now on the sPTT model, ε highly affects the shear-thinning behaviour of the fluid modeled and additionally controls its elongational characteristics by setting an upper bound to the extensional viscosity [45, 49, 50]. For the limiting case of $\varepsilon = 0$ then $f_A = 1$ and Eq. (7) reduces to the Oldroyd-B model, for which the extensional viscosity becomes unbounded above $\dot{\epsilon} = 1/(2\lambda)$, predicting an infinite extensional viscosity [51]. Combining Eqs. (7) and (9) it is straight forward to obtain:

$$\overset{\triangledown}{\mathbf{A}} = \begin{cases} -\frac{f_s}{\eta_p}\boldsymbol{\tau}_p, & \text{sPTT} \\ -\frac{1}{\eta_p}\boldsymbol{\tau}_p, & \text{FENE-P} \end{cases} \tag{10}$$

where $f_S = 1 + (\lambda\varepsilon/\eta_p)\mathrm{Tr}\boldsymbol{\tau}_p$ in the sPTT equation is the linear function f_A but now expressed in terms of the polymeric stress tensor, rather than the conformation tensor. Taking the upper convected derivative of the sPTT expression for the stress tensor given in Eq. (9) and using Eq. (10) we get:

$$\lambda\overset{\triangledown}{\boldsymbol{\tau}}_p + f_S\boldsymbol{\tau}_p = \eta_p\dot{\boldsymbol{\gamma}}, \tag{11}$$

where it was used that $\overset{\triangledown}{\mathbf{I}} = -\dot{\boldsymbol{\gamma}}$.

Examining now the FENE-P model, L^2 is used to relate the maximum length of a fully-extended dumbbell to its equilibrium length and is responsible for both the shear-thinning and the bounding plateau of the extensional viscosity [47, 52]. Following the same procedure as before, the expression of the FENE-P model in terms of the stress tensor can be written:

$$\lambda\overset{\triangledown}{\boldsymbol{\tau}}_p + f_F\boldsymbol{\tau}_p = \underline{\frac{\mathrm{D}f_F}{\mathrm{D}t}\left[\frac{\lambda}{f_F}\boldsymbol{\tau}_p + \frac{a\eta_p}{f_F}\mathbf{I}\right]} + a\eta_p\dot{\boldsymbol{\gamma}}, \tag{12}$$

where $f_F = 1 + [3a + (\lambda/\eta_p)\mathrm{Tr}\boldsymbol{\tau}_p]/L^2$ is the linear function of the trace of the polymer stress tensor. For any homogeneous flow, such as steady-state shear or planar/uniaxial extension, $\mathrm{D}f_F/\mathrm{D}t = 0$ and thus, the underlined term on the right-hand side of Eq. (12) will vanish with the FENE-P obtaining a similar expression to Eq. (11) of the sPTT model. Considering homogeneous flows and by taking the limit of $L^2 \to \infty$, then $f_F \to 1$ and $a \to 1$ and the FENE-P model reduces to the Oldroyd-B constitutive equation. Moreover, examining the analogy between f_S and f_F of the sPTT and FENE-P models, it is found that for $L^2 >> 3$ and $\varepsilon << 1$ the two models are expected to produce essentially identical behaviour when in homogeneous flows for $\varepsilon \sim 1/L^2$. Additional details can be found in [53].

Figure 2 illustrates the rheometric data for the fluids investigated and discussed in the next sections using the sPTT and the FENE-P models, highlighting their viscometric properties for different sets of parameters. More specifically, in Fig. 2a the extensional viscosity, η_e, scaled by the total viscosity is plotted when the fluid undergoes a homogeneous, steady-state, planar-extensional flow, for increasing $\lambda\dot{\epsilon}$. It can be seen that η_e increases monotonically for all cases until it reaches different plateaus for each particular case at approximately $\lambda\dot{\epsilon} \approx 5$. The value of this upper bound of η_e depends both on the value of the extensibility parameter (ε or L^2) and the solvent-to-total viscosity ratio (β). Furthermore, Fig. 2b provides the behaviour of the shear-viscosity under homogeneous, steady-state shear flow, for increasing values of $\lambda\dot{\gamma}$. It is clear that different scaled shear-rate values need to be applied in order for shear-thinning to become noticeable for each particular fluid. For the cases of the sPTT model with $\beta = 1/9$ and $\varepsilon = 0.01$, $\varepsilon = 0.05$ and $\varepsilon = 0.25$ the shear-thinning is large, where it is seen that the higher the value of ε, shear-thinning begins at lower shear-rates. On the contrary, for all the low concentration polymer solutions ($\beta = 0.95$) the shear-thinning of the fluid is negligible, remaining nearly constant and practically the total viscosity is dominated by the solvent viscosity (essentially constant shear-viscosity). The inset of Fig. 2a presents the ratio between the extensional-viscosity and the shear-rate dependent viscosity (known as the Trouton ratio), while the inset figure of Fig. 2b shows the ability of the two viscoelastic models to generate a non-monotonic, shear-thinning first normal-stress difference [22]. We mention here that the FENE-P model with $L^2 = 5000$ and the sPTT model with $\varepsilon = 0.0002$ for $\beta = 0.95$ are selected such that they follow the analogy discussed above between the two models and thus, as can be seen, to present essentially identical viscometric responses in homogeneous rheological flows.

The discretised set of partial differential equations (Eqs. (4) and (5)) are solved using an in-house implicit finite volume CFD solver, developed for collocated meshes, which is described in detail in Oliveira *et al.* [54] and Oliveira [55]. For enhanced stability and convergence properties we used the log-conformation approach [56] which solves the evolution of the logarithm of conformation tensor ($\boldsymbol{\Psi} = \log\mathbf{A}$), within a finite-volume methodology, as described in detail in Afonso *et al.*

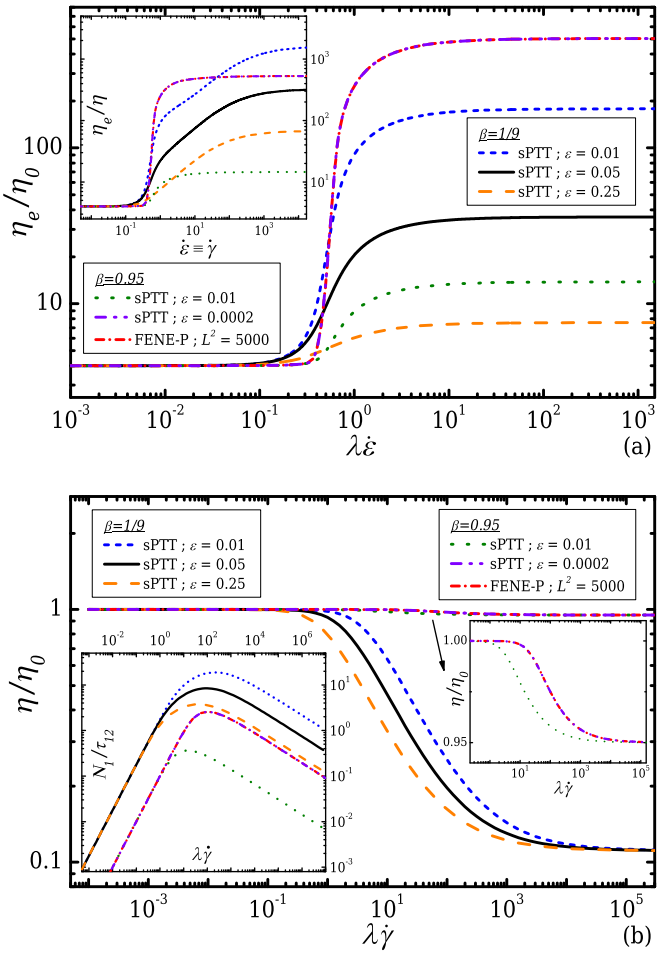

Figure 2: Rheometric properties of the sPTT model for $\beta = 1/9$ considering different extensibility parameters $\varepsilon = 0.01$, $\varepsilon = 0.05$ and $\varepsilon = 0.25$, for $\beta = 0.95$ with $\varepsilon = 0.01$ and $\varepsilon = 0.0002$, together with the case of the FENE-P model with $\beta = 0.95$ and $L^2 = 5000$. (a) Extensional viscosity (η_e) in steady extensional planar flow scaled by the total zero-shear viscosity, and (b) Shear viscosity (η) scaled by the total zero-shear viscosity. The inset in figure (a) shows the ratio between the extensional and the shear-rate dependent viscosity, while the inset figures in (b) show the first normal-stress differences in steady-shear flows scaled by the characteristic total shear-stress and a zoomed view of the scaled shear-viscosity curve for $\beta = 0.95$.

Table 1: Characteristics of the meshes discretising the 3D e-VROC^{TM} geometry.

Mesh	$\delta x_{min}/w_u$	$\delta y_{min}/w_u$	$\delta z_{min}/w_u$	#Computational Cells
M0	~0.007	~0.007	0.005	180180
M1	~0.005	~0.005	0.004	466956

[48, 57]. Here the evolution of the logarithm of the conformation is given in the FENE-P form:

$$\frac{\partial \boldsymbol{\Psi}}{\partial t} + \mathbf{u}\cdot\nabla\boldsymbol{\Psi} - (\boldsymbol{\Omega}\boldsymbol{\Psi} - \boldsymbol{\Psi}\boldsymbol{\Omega}) - 2\mathbf{B} = -\frac{1}{\lambda}(f_A\mathbf{I} - a\mathrm{e}^{-\boldsymbol{\Psi}}), \quad (13)$$

where $\boldsymbol{\Omega}$ is a pure rotational component and $\mathbf{B}$ a traceless extensional component. The sPTT equation is recovered when $a \equiv f_A$ and as given in Eq. (8). For further details and an in depth analysis the reader is addressed to the previous references. The pressure and velocity fields are coupled using the SIMPLEC algorithm for collocated meshes by employing the Rhie and Chow interpolation technique [58]. The convective terms both in the momentum and the evolution equation of the logarithm of the conformation tensor, are discretised using the CUBISTA high-resolution scheme [59], while all diffusive terms are evaluated with central differences. All the calculations here were carried out at a vanishing Reynolds number, $\mathrm{Re} \to 0$ (creeping flow conditions are imposed by dropping out the convective term, $\mathbf{u}\cdot\nabla\mathbf{u}$, in the momentum equation to be identically zero, Eq. (5)). Full 3D numerical meshes that discretise the e-VROC^{TM} geometry have been employed (details in Table 1) in order to solve numerically the discretised equations. Figure 3 shows meshes M0 and M1, with the latter being employed in the majority of the simulations.

A useful parameter to characterise the flow type is employed, which allows us to discuss our results and demonstrate the potential efficiency of e-VROC^{TM} in terms of extensional rheometry experiments. The flow-type parameter, ξ, is defined as

$$\xi = \frac{\|\boldsymbol{D}\| - \|\boldsymbol{\Omega}\|}{\|\boldsymbol{D}\| + \|\boldsymbol{\Omega}\|}, \quad (14)$$

where $\|\boldsymbol{D}\| = (\frac{\boldsymbol{D}:\boldsymbol{D}^{\mathrm{T}}}{2})^{1/2}$ is the magnitude of the rate-of-deformation tensor, $\boldsymbol{D} = \frac{1}{2}[\nabla u + (\nabla u)^{\mathrm{T}}]$, and $\|\boldsymbol{\Omega}\| = (\frac{\boldsymbol{\Omega}:\boldsymbol{\Omega}^{\mathrm{T}}}{2})^{1/2}$ is the magnitude of the vorticity tensor, $\boldsymbol{\Omega} = \frac{1}{2}[\nabla u - (\nabla u)^{\mathrm{T}}]$. Based on the velocity field that is evaluated from the CFD simulations, the ξ parameter is then calculated within the entire domain and it can be seen from Eq. (14) that it varies within the range $[-1, 1]$. For $\xi = -1$, the flow is considered as rotational (solid-body like), while for $\xi = 1$ the flow is characterised as pure extension. When $\xi = 0$ the flow is simple shear [60, 61].

4. Results and discussion

In this section we report our numerical results for both Newtonian and viscoelastic fluid flows in the e-VROC^{TM} geometry. Initially we present the response of a Newtonian fluid, which we consider the "base" flow and provides a basic understanding of

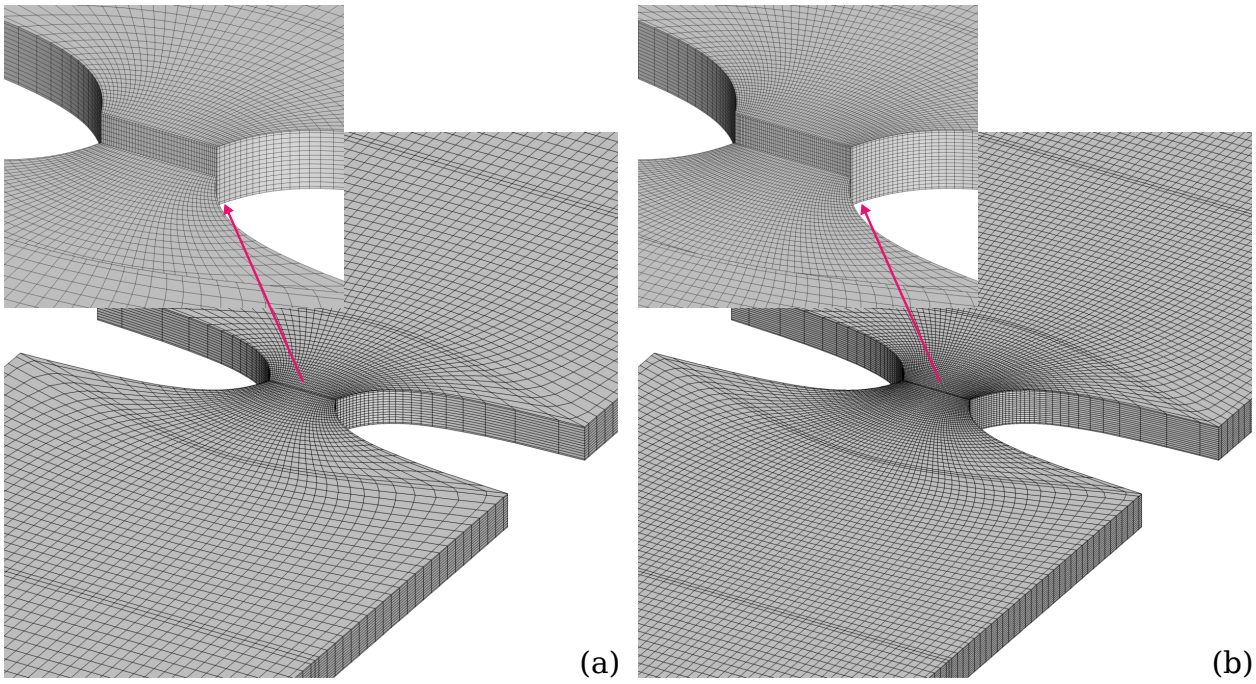

Figure 3: Three-dimensional computational meshes used to discretise the e-VROC^{TM} geometry (a) M0 and (b) M1, together with a zoomed view at the throat of the contraction/expansion.

the abilities of the e-VROC^{TM} configuration to generate extensional flow. Then the flow characteristics of viscoelastic fluid flows described by the sPTT and the FENE-P models are analysed and are compared to the Newtonian case. Following that, the results from pressure-drop measurements are presented following the same approach of Ober *et al.* [24] and finally, flow and stress fields obtained numerically within the e-VROC^{TM} geometry are shown for various model parameters.

4.1. Newtonian fluids

As discussed in Section 2, the rationale behind the e-VROC^{TM} geometry being used in extensional rheological measurements are focused on its potential ability to generate a region of constant strain-rate along the flow centreline, where the flow is purely extensional. Here, we assess this ability by presenting the results obtained from the numerical simulations of the generic flow of a Newtonian fluid flow, when considering creeping flow conditions (Re $\rightarrow$ 0).

Figure 4 presents the velocity and strain-rate profiles along the flow centreline in the e-VROC^{TM} geometry, which are directly compared with the desired theoretical profiles discussed in Section 2. The theoretical velocity profile is evaluated as in White [62] for rectangular cross-sections, considering that the flow along the constriction is everywhere fully developed. More specifically, Fig. 4a illustrates the normalised streamwise velocity profile obtained numerically, together with an inset figure that contains a contour-plot of the normalised streamwise velocity (u-component). A slice along the $xy-$plane is taken through the 3D geometry so that the flow centreplane of the e-VROC^{TM} geometry is shown, with the *dashed-line* indicating the centreline where the velocity and strain-rates are taken. Examining the velocity profile, it can be seen that significant deviations exist compared to the desired response. Clearly, as the fluid approaches the converging part of the constriction its velocity starts to increase earlier compared to the ideal profile, due to viscous diffusion of momentum and affected by entrance effects. This occurs around $x/H_2 \approx -8$, which corresponds to approximately four contraction lengths ($4l_c$), and not at the desired location of $x/H_2 = 0$. Similar behaviour has also been reported in the experimental paper of Ober *et al.* [24]. As Newtonian creeping-flow is linear and reversible, the exact same behaviour is also observed in the diverging part. Moreover, it can be seen that the maximum velocity obtained at the throat of the constriction deviates considerably when compared to the theoretical value, reaching an approximate deviation of 14% (below the theoretical). This can be explained by the fact that the transition length (l_c) considered in the design of the converging part (and the diverging) is small and the fluid cannot develop the desired velocity, which corresponds to the value of the fully-developed profile at this cross-section. Hence, the assumption of obtaining a fully-developed flow which is additionally defined with specific characteristics (linear increase of velocity) cannot be supported for this particular configuration, but on the contrary non-homogeneous flow appears to occur. We believe that this drawback is directly related to the employed length of the contraction/expansion region. This has also been discussed in Zografos *et al.* [41] for an optimisation study of converging/diverging channels. In their study, as the length of the contraction reduces, the optimisation procedure generated geometries that demonstrated large shape deviations from the hyperbolic design at the start of the converging region. Obtaining the specific/desired behaviour, could only be achieved by modifying the boundaries of the designs and generating appropriate transition regions upstream and downstream of the constriction. Here, the deviations occurring in the velocity profiles along the flow centreline between the ideal and the one produced by e-VROC^{TM}, have consequently a direct effect on the generated strain rate, where, as it can be seen in Fig. 4b, the response is not the desired one. It is important to highlight that, in contrast with Ober *et al.* [24], here we report a velocity

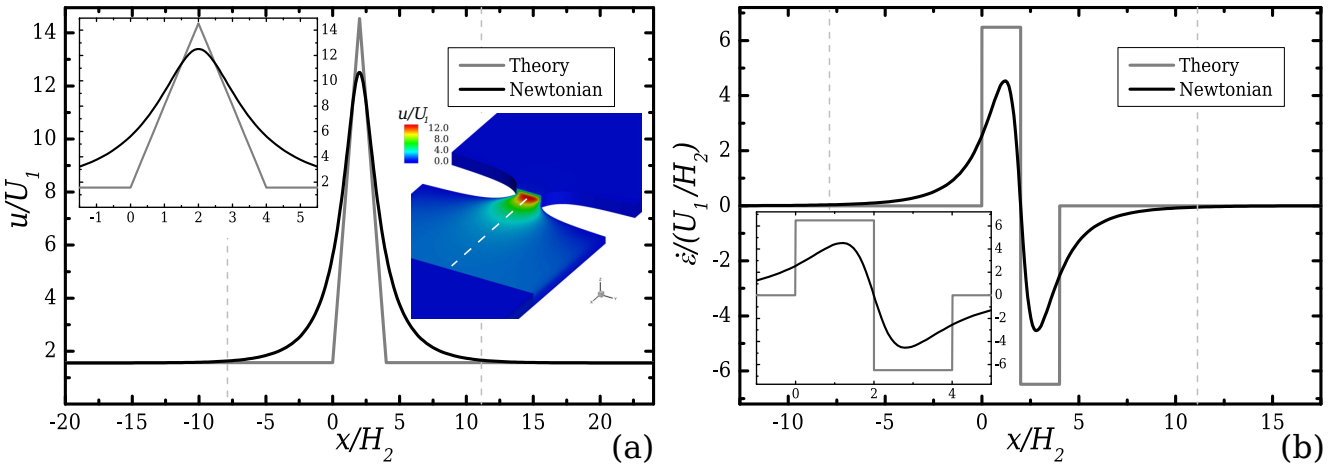

Figure 4: Normalised velocity (a) and normalised strain-rate (b) profiles along the centreline of the flow in the e-VROC^{TM} geometry for a Newtonian fluid flow under creeping-flow conditions (Re $\rightarrow$ 0). The vertical *dashed* lines indicate the locations of the pressure sensors P_2 and P_3 placed on the e-VROC^{TM} geometry originally by Ober *et al.* [24], also schematically shown in Fig. 1a, while the theory (ideal) velocity and strain-rate profiles are explained in Fig. 1c and d respectively. Contours of the normalised streamwise velocity (u-component) for a Newtonian fluid in the e-VROC^{TM} geometry are included in (a) as an inset figure, where the *dashed-line* illustrates the flow centreline where profiles are evaluated.

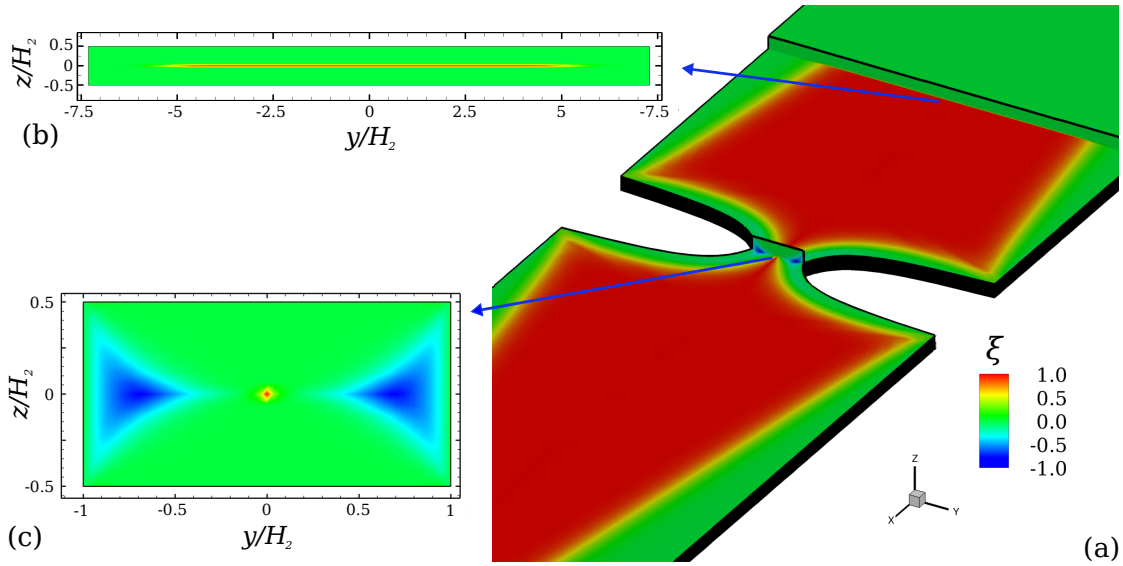

Figure 5: Flow-type parameter for a Newtonian fluid flow at Re → 0 in the e-VROC^{TM} geometry along the centreplane (a). Zoomed figures demonstrate its values at yz-planes upstream of the flow (b) and at the throat of the contraction/expansion (c).

profile with a lower maximum velocity along the flow centreline than predicted by theory (by ~ 30%), whereas Ober *et al.* [24] observed the opposite behaviour. This is most likely due to a "scalloping" feature of the wet-etching process, as Ober *et al.* [24] highlight in their study. More details on this issue are discussed in Appendix A.

In order to investigate the convergence with mesh refinement of our numerical solutions, two numerical meshes M0 and M1 (details given in Table 1) were used for discretising the physical domain. Comparing the results obtained between the two grids, a good agreement was found (cf. Table 2). Particularly a negligible maximum deviation of 0.25% was found for the developed maximum velocity along the flow centreline, whereas a minor deviation of 0.71% is reported for the resulting strain-rate at the throat of the contraction/expansion. Also a small deviation of 2.0% occurs at the evaluation of ΔP_c while the pressure coefficient deviates slightly (0.68%).

The solution of the flow field obtained under creeping-flow conditions from the numerical simulations, can be further used to provide an indication of the levels of extensional flow that the e-VROC^{TM} geometry generates using the flow-type parameter ξ, as discussed in Section 3. In particular, when $\xi = 1$ the flow is extensional dominated, when $\xi = 0$ it is shear dominated, while for $\xi = -1$ the flow approaches solid-body rotation. Figure 5 illustrates the contour-plots of the evaluated flow parameter for the e-VROC^{TM} geometry, where it can be seen that a region of high extension exists along the flow centreline. However, this is actually achieved only for a very thin region around the centreplane as can be seen by the yz-slices taken at an upstream location of the contraction (cf. Fig. 5b) and at the middle of the contraction (cf. Fig. 5c). The fact that the high extensional region is restricted to a very narrow region around the

Table 2: Comparison between the results obtained for the two meshes employed for a range of different cases.

Fluid	Wi	u	$\dot{\epsilon}$	ΔP_c	$\mathcal{P}$
Newtonian	0	0.25%	0.71%	2.00%	0.68%
sPTT	0.5	0.48%	1.02%	2.28%	0.76%
($\varepsilon = 0.05$)	5	0.23%	0.22%	2.99%	0.94%
	15	0.34%	0.74%	2.54%	0.85%
	25	0.50%	0.83%	2.23%	0.78%
sPTT	5	0.11%	0.40%	1.95%	0.69%
($\varepsilon = 0.0002$)	15	0.14%	0.66%	1.81%	0.65%
FENE-P	5	0.09%	0.04%	1.93%	0.68%
($L^2 = 5000$)	10	0.02%	1.00%	1.79%	0.64%
	15	0.41%	1.25%	1.82%	0.65%

* The deviation reported for u and $\dot{\epsilon}$ for each case is evaluated using their maximum obtained values.
** ΔP_c and $\mathcal{P}$ are evaluated as discussed in Section 2, following the same procedure of Ober *et al.* [24]

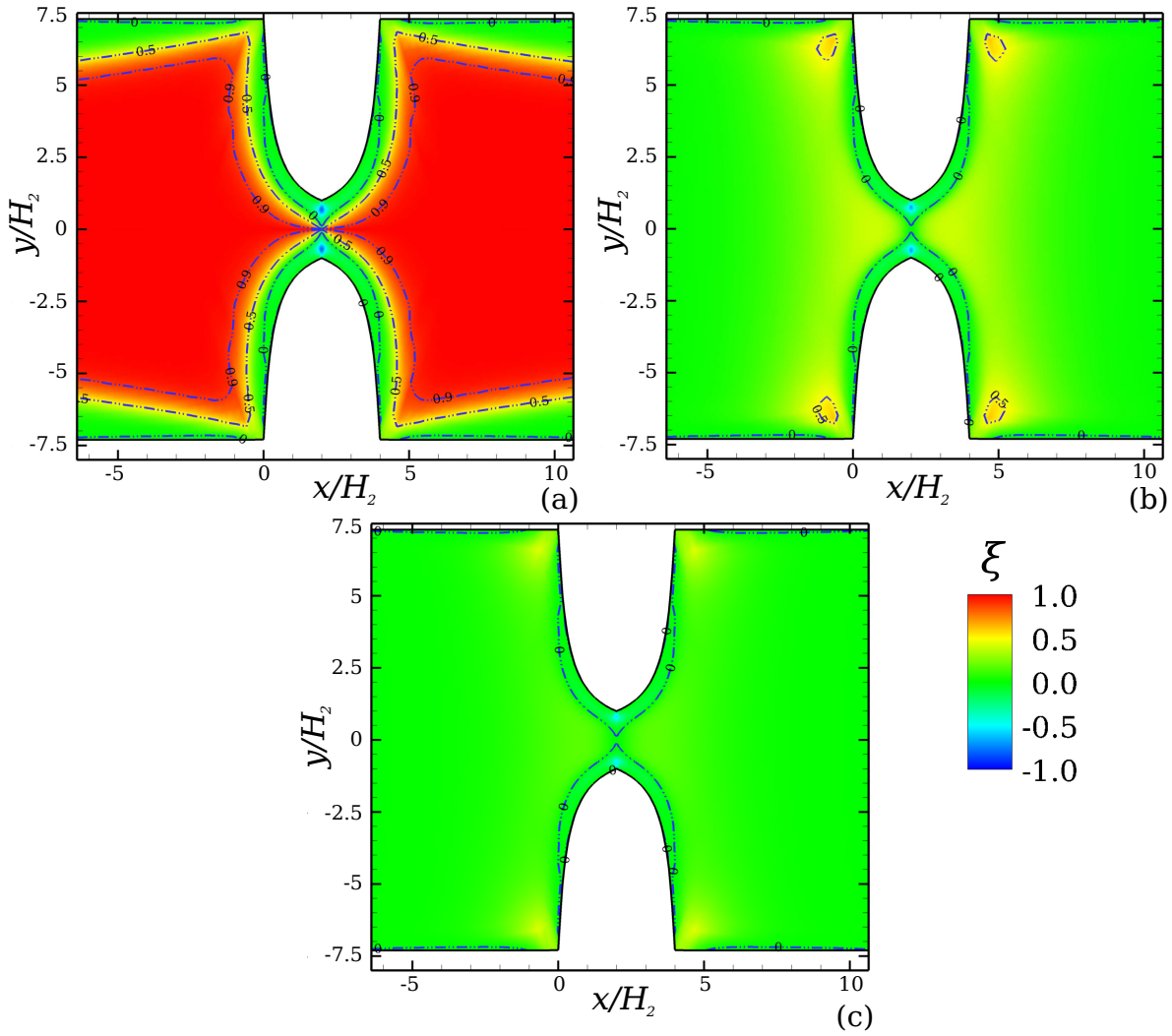

Figure 6: Flow-type parameter for a Newtonian fluid at Re $\rightarrow$ 0 in the e-VROC^{TM} geometry at different z-planes: (a) centreplane, (b) $\sim$ 12% away from centreplane, (c) $\sim$ 24% away from centreplane. The dashed-lines correspond to the indicated contour values.

centreplane, is further verified by examining the contours of the flow-type parameter at different locations as shown in Fig. 6. The ξ contour-plots along the centreplane, shown in Fig. 6a, indicate an apparent strong extension region. However, at approximately 12% and 24% away from centreplane, as shown in Fig. 6b and Fig. 6c respectively, it can be seen that the flow is shear dominated. Thus from a volume-average perspective, the e-VROC^{TM} geometry would appear to be essentially a shear-dominated flow device due to its small depth aspect ratio.

At this point, and before examining the behaviour of viscoelastic fluids within the e-VROC^{TM} geometry, it is worth examining how the configuration differs from the responses produced by two equivalent geometries that have an abrupt contraction/expansion shape. In order to do this we employed two geometries that are defined with the same geometrical characteristics as e-VROC^{TM}, but are designed with a long and a short contraction/expansion length. The long-abrupt (L) constriction has a total length $l_L = 2l_c$, while the short-abrupt (S) constriction has a length $l_S = l_c/18.5$. In Fig. 7 the comparison between all three designs is provided. Figure 7a demonstrates the contours of the normalised streamwise velocity along the centreplane of the e-VROC^{TM} configuration, while Fig. 7b and Fig. 7c show the equivalent behaviour in the long and short sudden contraction/expansion designs respectively. The normalised velocity profile along the flow centreline for each one of the configurations is shown in Fig. 7d. For the long design it can be seen that although the abrupt constriction has an impact on the centreline velocity, due to viscous diffusion of momentum and entrance and exit effects, at approximately the same locations as in e-VROC^{TM}, the actual velocity is substantially affected reaching higher values than those achieved in the e-VROC^{TM}. Along the constriction the fluid manages to reach the expected theoretical maximum velocity for a channel with AR = 2 ($u/U_1 \simeq 14.5$) [62], due to the sufficiently long length that enables the flow to become fully developed. Clearly, as can be seen in Fig. 7e, this behaviour results in a strain-rate that is not desirable, since it reaches the absolute maximum values upstream and downstream of the constriction. Examining now the

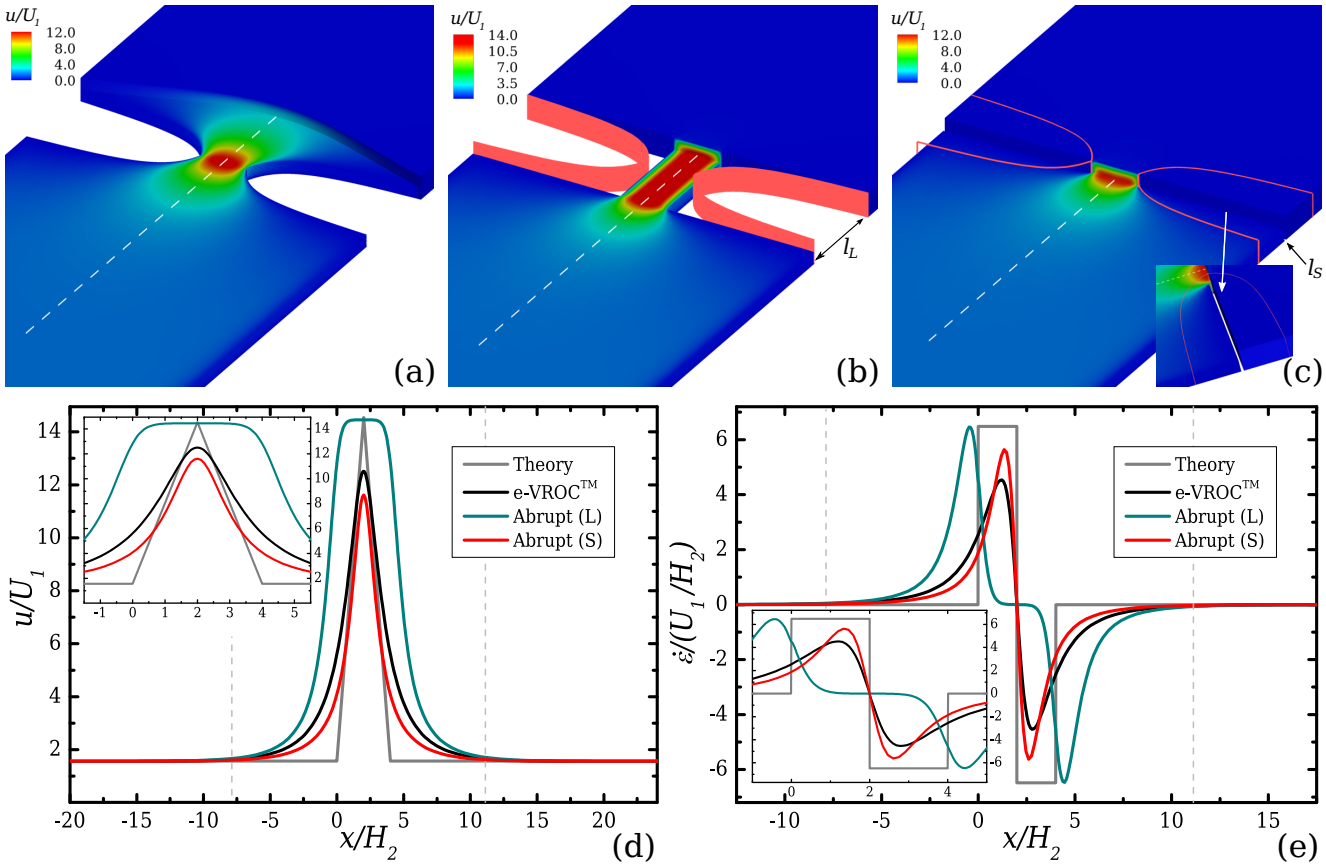

Figure 7: Contours of the normalised streamwise velocity (u-component) for a Newtonian fluid in (a) the e-VROC^{TM} geometry, (b) an abrupt contraction/expansion geometry with $l_L = 2l_c$ and (c) an abrupt contraction/expansion geometry with $l_S = l_c/18.5$. Normalised velocity (d) and strain-rate (e) profiles along the centreline of the flow for all geometries. The dashed line included in all contour-plots indicates the centreline where the profiles are extracted. In (b) and (c) the shape of e-VROC^{TM} is added for comparison purposes, while in (c) a zoomed view of the right half section of the contraction/expansion is also provided. In (d) and (e) the vertical *dashed* lines indicate the locations of the pressure sensors P_2 and P_3 placed on the e-VROC^{TM} geometry originally by Ober *et al.* [24] (see Fig. 1a), while the theory (ideal) velocity and strain-rate profiles are explained in Fig. 1c and d respectively.

equivalent behaviour for the short abrupt contraction/expansion case, it can be seen that the centreline velocity starts to increase in a similar manner as in the two other cases. However, it is clearly affected from the fact that now the constriction begins further downstream and thus the velocity profile reaches relatively lower values compared to the ones observed in the e-VROC^{TM} device, being closer to the ideal. Overall, the resulting behaviour is not very different from the one produced by e-VROC^{TM} device, with the applied strain rate reaching to a slightly higher value due to the fact that the centreline velocity is increased more rapidly.

4.2. *Viscoelastic fluids*

The behaviour of the viscoelastic fluids described by the simplified linear sPTT and the FENE-P models is presented here for a range of Weissenberg numbers, defined as $\mathrm{Wi} = \lambda U_2/H_2$ (cf. Section 2). We also report our results considering an "effective" Weissenberg number that is defined as $\mathrm{Wi}_{\mathrm{eff}} = (1-\beta)\mathrm{Wi}$, in order to take into account any solvent contributions to the viscous stresses [63, 64].

We start with the results obtained for the case of the more concentrated polymers described by the sPTT model with $\beta =$ 1/9 and $\varepsilon = 0.01$, 0.05 and 0.25. The performance of the e-VROC^{TM} geometry obtained for these cases is shown in Fig. 8 in terms of the centreline normalised velocity and strain-rate profiles. The behaviour of the Newtonian fluid described previously, together with the desired theoretical velocity and the strain rate profiles are also included for comparison purposes. As was discussed in Section 3 and shown in Fig. 2, the different values considered for the extensibility parameter ε result in fluids that differ in their elastic properties (as ε decreases, elasticity of the fluid in terms of maximum first normal-stress difference increases) and in their shear-thinning behaviour (as ε increases shear-thinning begins at lower shear-rates). Starting from the least elastic case, of $\varepsilon = 0.25$, Fig. 8a demonstrates the behaviour of the normalised streamwise velocity along the flow centreline for a range of Weissenberg numbers, while Fig. 8b shows the corresponding normalised strain-rate profiles along the length of the converging/diverging region of a fluid element flowing along the flow centreline. It can be seen that for all Weissenberg numbers investigated the velocity profile is reduced compared to the Newtonian behaviour and thus a larger deviation occurs from the desired profile, due to the shear-thinning nature of the fluid (the flow becomes more plug-

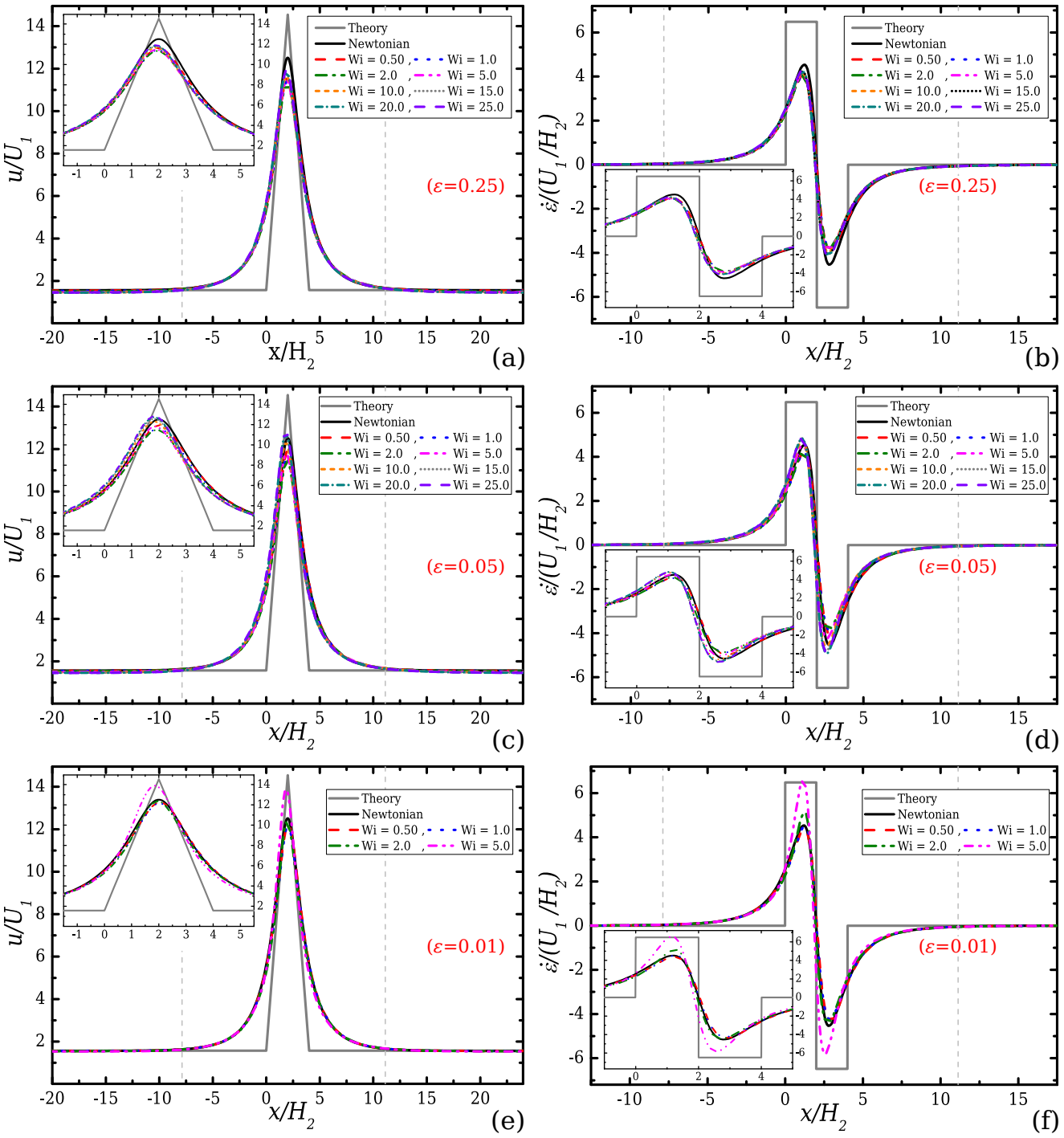

Figure 8: Normalised velocity (a, c, e) and normalised strain-rate (b, d, f) profiles along the centreline of the flow in the e-VROC^{TM} geometry for the sPTT model with with $\beta = 1/9$ and $\varepsilon = 0.25$ (a, b), $\varepsilon = 0.05$ (c, d) and $\varepsilon = 0.01$ (e, f), under creeping-flow conditions. The vertical *dashed* lines indicate the locations of the pressure sensors P_2 and P_3 placed on the e-VROC^{TM} geometry originally by Ober *et al.* [24] (see Fig. 1a), while the theory (ideal) velocity and strain-rate profiles are explained in Fig. 1c and d respectively.

like with increasing shear-thinning). Additionally, for Wi $\gtrsim 5$ an overshoot in the velocity is observed (although it is so small that it is hard to discern in the plot). The overshoot starts to form in the throat of the contraction/expansion and its intensity increases for increasing Wi, demonstrating the effects of elasticity on the flow kinematics. This response of the velocity due to the elasticity of the fluid together with the shear-thinning behaviour affects the developed strain-rate, which in turn under-predicts the desired response and additionally exhibits mild overshoots. Velocity overshoots in contractions, expansions or contraction/expansion flows, with abrupt or smooth boundaries, are not new and have been reported in the literature in a range of studies considering viscoelastic fluids, both numerically [21, 26, 28, 29, 41, 65–67] and experimentally [68].

Moreover, for the specific case of $\varepsilon = 0.25$ where the shear-thinning behaviour strongly influences the characteristics of the flow, it was shown in Zografos *et al.* [41] that even for a converging/diverging channel optimised for a Newtonian fluid flow, the desired homogeneous response along the flow centreline is not straight-forward to obtain.

Decreasing the value of the ε parameter leads to a similar behaviour. More specifically, in Fig. 8c shows the normalised velocity for the case of $\varepsilon = 0.05$, and similar conclusions can be drawn. However, for this case the formation of the overshoot for Wi $\gtrsim 5$ is even more pronounced due to the more elastic behaviour compared to the case with $\varepsilon = 0.25$ (see fluid properties

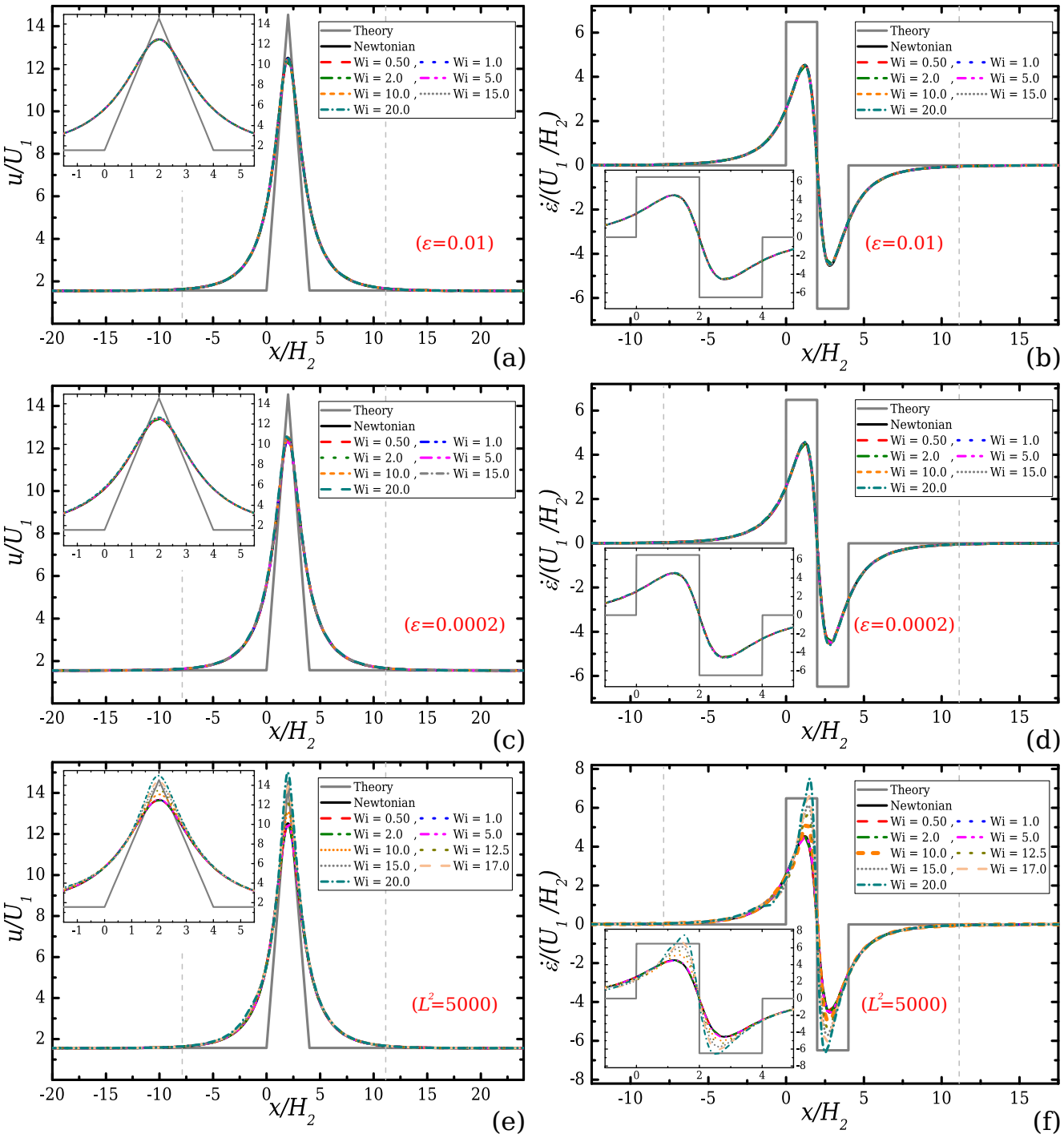

Figure 9: Normalised velocity (a, c, e) and normalised strain-rate (b, d, f) profiles along the centreline of the flow in the e-VROC^{TM} geometry for the sPTT model with $\varepsilon = 0.01$ (a, b) and $\varepsilon = 0.0002$ (c, d) and the FENE-P model with $L^2 = 5000$ (e, f), all for $\beta = 0.95$ under creeping-flow conditions. The vertical *dashed* lines indicate the locations of the pressure sensors P_2 and P_3 placed on the e-VROC^{TM} geometry originally by Ober *et al.* [24] (see Fig. 1a), while the theory (ideal) velocity and strain-rate profiles are explained in Fig. 1c and d respectively.

in Fig. 2). Now, the velocity overshoot reaches higher values than the maximum velocity that is observed for the Newtonian fluid in the throat of the device. In Fig. 8d, the scaled strain-rate is shown for this particular case, where the effects of the velocity overshoot are now more clear and the deviation from the desired behaviour is again obvious. As the fluid becomes more elastic, with $\varepsilon = 0.01$, it can be seen in Fig. 8e that the velocity overshoots start to form at smaller Weissenberg numbers (Wi $\gtrsim$ 2). As Wi increases even further, and in particular for Wi = 5, a large velocity overshoot of about 12% compared to the Newtonian profile is observed close to the throat of the converging/diverging contraction. These overshoots are now clearly affecting even more the applied strain-rate, which is notably increased along the length of the converging/diverging contraction with a maximum deviation of 44% compared to the equivalent Newtonian profile, as can be seen in Fig. 8f. At this Weissenberg number (Wi = 5) small oscillations of the lateral velocity (v-velocity) at the throat of the contraction/expansion along the flow centreline around the expected zero-value have been observed, exhibiting a small root-mean-square (RMS) value of $V_{\mathrm{RMS}}/U_2 = 0.001$. The RMS of a generic variable ϕ is here evaluated as $\phi_{\mathrm{RMS}} = \left[({\phi_1}^2 + {\phi_2}^2 + .. + {\phi_n}^2)/n\right]^{1/2}$ for a time-series of n equidistant sampling points. These oscillations do not affect the streamwise u-velocity, for which the RMS deviation of the fluctuations around its time averaged value $\langle u \rangle$ (i.e. $U'_{\mathrm{RMS}} = (u - \langle u \rangle)_{\mathrm{RMS}}$) along the flow centreline was found to be at most $U'_{\mathrm{RMS}}/U_2 = 0.0008$ over the same time period. Further increases of Weissenberg number result in a clear time-dependent flow as will be discussed in detail later in Section 4.4.

Investigating the cases of more representative dilute polymer solutions ($\beta = 0.95$), described by the sPTT model with $\varepsilon = 0.01$ and $\varepsilon = 0.0002$, and the FENE-P model with $L^2 = 5000$, similar observations can be made. Figure 9 presents the behaviour of the normalised streamwise velocity and the equivalent strain-rate along the flow centreline, for each particular case with increasing Weissenberg numbers. More specifically, examining the case of the sPTT model with $\varepsilon = 0.01$ shown in Fig. 9a, it can be seen that the flow is almost Newtonian-like. There are virtually no differences observed when compared to the Newtonian case, in contrast to the equivalent highly concentrated case ($\beta = 1/9$) with $\varepsilon = 0.01$ where the shear-thinning and fluid's elasticity highly affected the flow field. By reference to Fig. 2, it can be seen that the shear-thinning is small for this case and additionally the fluid's elasticity cannot drastically influence the flow field for this range of Wi considered. These responses are further verified by the resulting strain-rates shown in Fig. 9b where for increasing Wi the differences with the Newtonian response are again negligible. Increasing further the elasticity of the fluid, by reducing the extensibility parameter to $\varepsilon = 0.0002$, while shear-thinning is still negligible (cf. Fig. 2), very small velocity overshoots are observed above Wi = 10, as shown in Fig. 9c. These overshoots are smooth, a fact that is verified by the resulting strain-rates profiles shown in Fig. 9d, where for increasing Wi the differences with the Newtonian response are not distinguishable. On the contrary, for the FENE-P model with $\beta = 0.95$ and $L^2 = 5000$ the elastic effects on the flow field within the e-VROC$^{\mathrm{TM}}$ geometry are more pronounced. The normalised streamwise velocity shown in Fig. 9e and consequently the normalised strain-rate, demonstrate the existence of large overshoots along the flow centreline above Wi = 5. The analogy between the FENE-P and the sPTT models ($\varepsilon \sim 1/L^2$; cf. Section 3) indicates that the FENE-P model with $L^2 = 5000$ has identical viscometric properties with the sPTT model for $\varepsilon = 0.0002$ when subjected to a homogeneous flow. Hence, the differences that are observed here between the two models is another indication of a non-homogeneous flow that is generated in the e-VROC$^{\mathrm{TM}}$geometry and particularly close to the constriction.

4.3. Pressure-drop measurements

Figure 10 presents the normalised pressure difference and the normalised first normal-stress difference along the flow centreline, with the latter including both the polymeric and the solvent contributions for all the cases investigated. As previously, the Newtonian behaviour is included in all figures for comparison. The pressure difference is evaluated as $\Delta P = P - P_{ref}$, where P is the pressure obtained along the flow centreline and P_{ref} is a reference pressure taken at $x/H_2 = -300$. The strongly shear-thinning nature of the sPTT model with $\beta = 1/9$, gives rise to a decrease of the pressure-drop in comparison with the Newtonian fluid which is clear in Fig. 10a for $\varepsilon = 0.25$, Fig. 10c for $\varepsilon = 0.05$ and Fig. 10e for $\varepsilon = 0.01$. More importantly, it can be observed that as Wi is increased the effect of the constriction upon the developed pressure-drop appears to vanish, resulting in a pressure-drop profile that is similar to what would occur for a flow in a straight channel. At this point it should be mentioned that, the closed-form viscoelastic models used here often fail to predict accurately the experimentally observed pressure-drop in contraction and other complex flows. This is a well known drawback of viscoelastic numerical studies using such differential-type models [20, 22, 41, 57, 66], that is in contrast to experimental measurements for viscoelastic fluid flows in contraction/expansion geometries which typically show a pressure-drop enhancement and an additional flow resistance due to the constriction [15, 34, 68, 69].

Similar to the behaviour of the pressure-drop, the first normal-stress difference ($(\tau_{11} - \tau_{22})/(\eta_0 U_2/H_2)$) is also influenced by the shear-thinning characteristics of the sPTT model. Figure 10b shows the behaviour of the normal-stress difference along the flow centreline for $\varepsilon = 0.25$ and it can be seen that for increasing Wi the first normal-stress differences are lower than those obtained for the Newtonian fluid (Wi = 0). This behaviour was also reported in Alves *et al.* [59] and is a consequence of the shear-thinning embedded in the rheological model. A similar response is also encountered for the case of $\varepsilon = 0.05$, as presented in Fig. 10d with slightly higher first normal-stress difference values in the converging/diverging constriction. However, as the maximum value of the first normal-stress difference of the fluid is increased by decreasing ε, higher normal-stress differences are encountered for all the cases examined, as can also be seen for the case of $\varepsilon = 0.01$ in Fig. 10f.

Examining now the responses of the dilute polymer solutions ($\beta = 0.95$) shown in Fig. 11 for the sPTT model with $\varepsilon =$

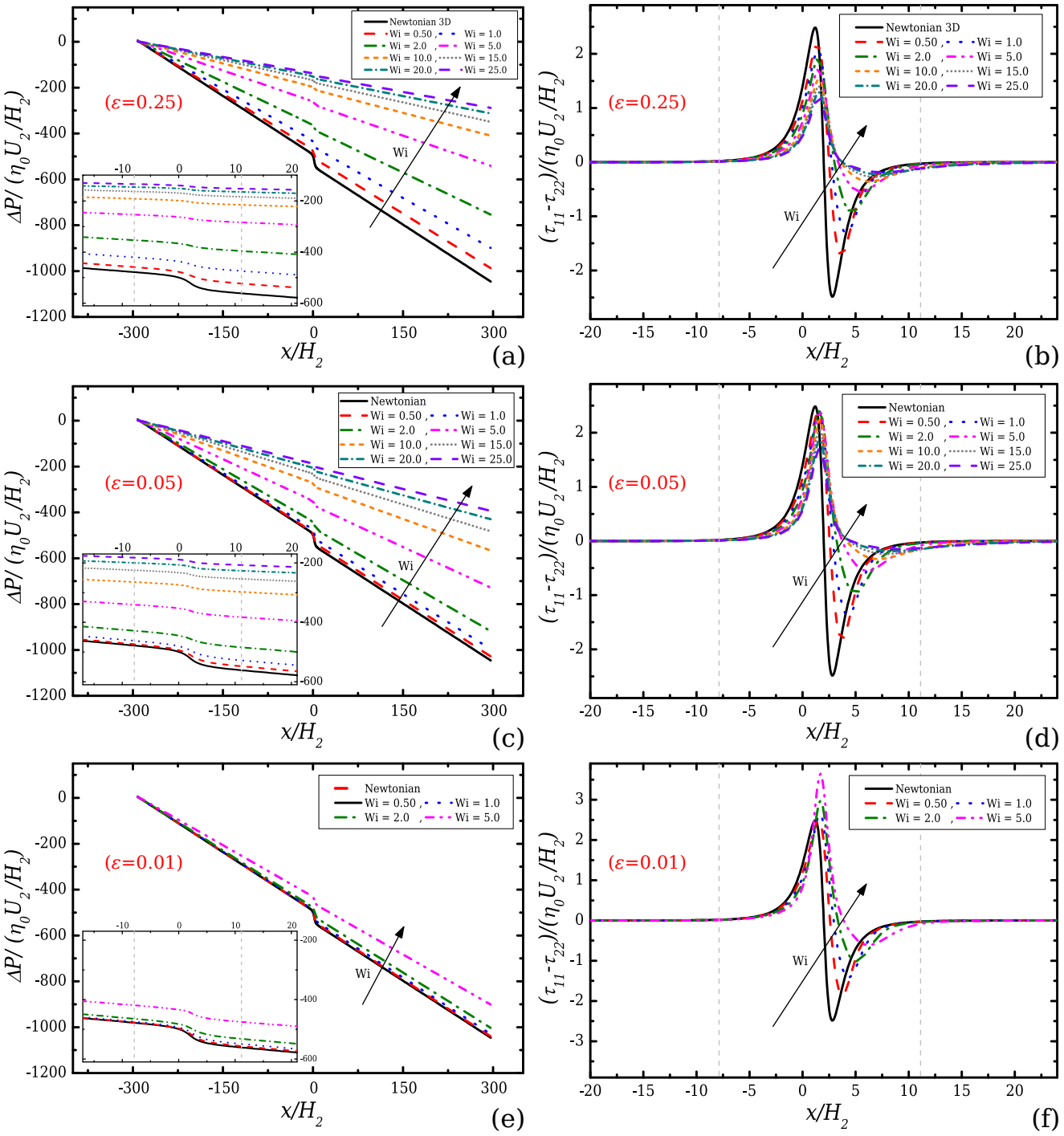

Figure 10: Normalised pressure difference (a, c, e) and normalised first normal-stress difference (b, d, f) profiles along the centreline of the flow in the e-VROC^{TM} geometry for sPTT model with $\beta = 1/9$ and $\varepsilon = 0.25$ (a, b), $\varepsilon = 0.05$ (c, d) and $\varepsilon = 0.01$ (e, f), under creeping-flow conditions. The vertical *dashed* lines indicate the locations of the pressure sensors P_2 and P_3 placed on the e-VROC^{TM} geometry originally by Ober *et al.* [24] (see Fig. 1a).

0.01 and $\varepsilon = 0.0002$, and the FENE-P model with $L^2 = 5000$, it can be seen that the cases of the sPTT model have a Newtonian-like behaviour both for the pressure-drop and in the first-normal-stress difference, further supporting our previous observations. On the contrary, the FENE-P model demonstrates a slight pressure-drop enhancement and overshoots in the first normal-stress difference with increasing Wi, further supporting the influence of the constitutive equation, as a result of the non-homogeneous flow along the centreline in the hyperbolic contraction/expansion.

Figure 12 presents the variation of the normalised pressure-drop along the hyperbolic constriction, for all fluids considered in this work. More specifically, Fig. 12a presents the variation of the pressure-drop along the contraction/expansion of

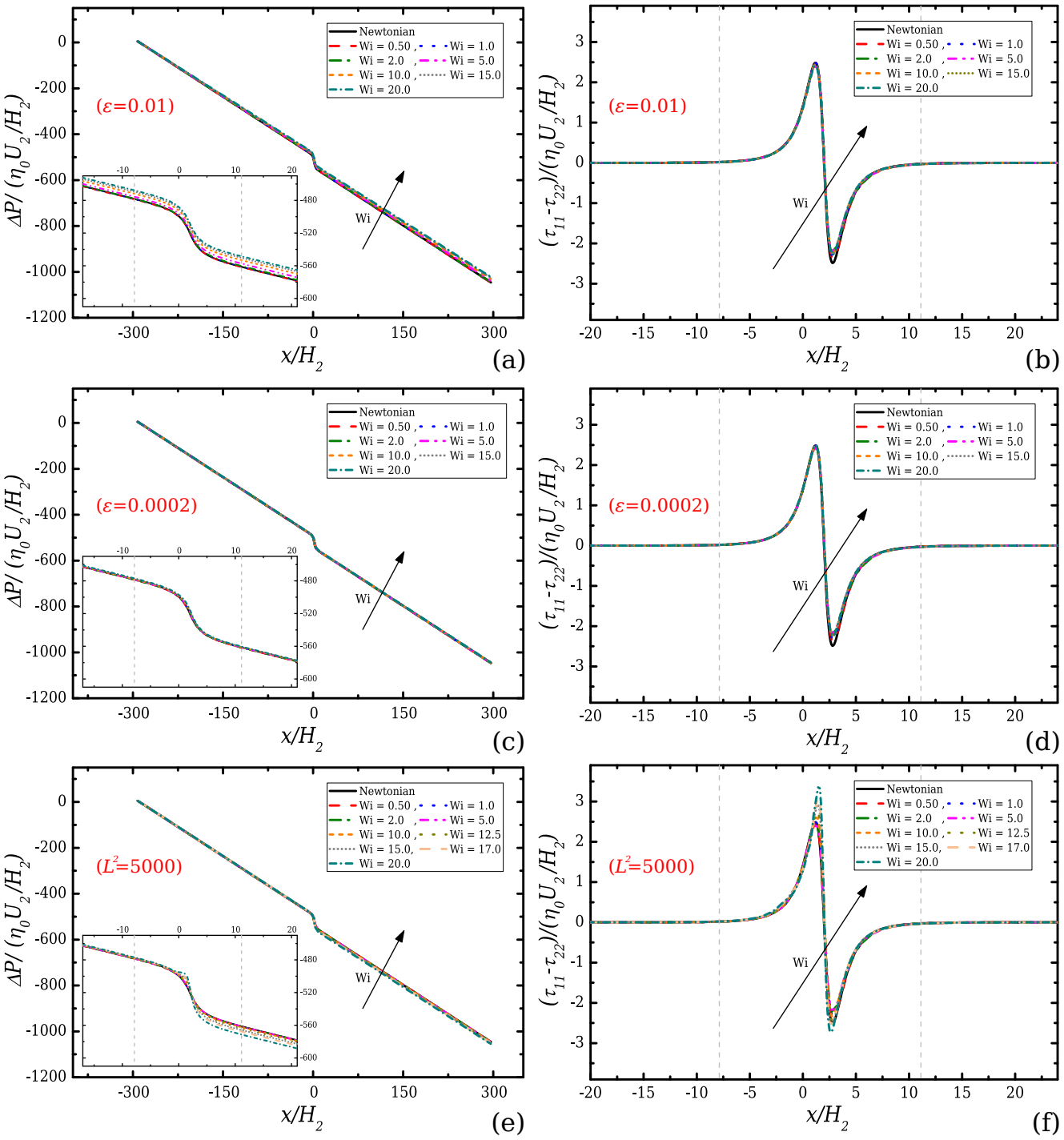

Figure 11: Normalised pressure difference (a, c, e) and normalised first normal-stress difference (b, d, f) profiles along the flow centreline of the e-VROC^{TM} geometry for the sPTT model with $\varepsilon = 0.01$ (a, b) and $\varepsilon = 0.0002$ (c, d) and the FENE-P model with $L^2 = 5000$ (e, f), all for $\beta = 0.95$ under creeping-flow conditions. The vertical *dashed* lines indicate the locations of the pressure sensors P_2 and P_3 placed on the e-VROC^{TM} geometry originally by Ober *et al.* [24] (see Fig. 1a).

the e-VROC^{TM} device for increasing Wi, while in Fig. 12b the same variation is provided, but as a function of the effective Weissenberg number. The pressure drop along the contraction/expansion is evaluated using Eq. (1), which is the same approach used in Ober *et al.* [24]. For the more concentrated polymer solutions ($\beta = 1/9$) simulated with the sPTT model, the predicted pressure-drops across the constriction are smaller when compared to the Newtonian fluid (dashed line), particularly for higher Wi. The difference with the Newtonian behaviour increases as ε is increased, due to the fact that the shear-thinning sets in at lower shear rates. On the other hand, for dilute polymer solutions with $\beta = 0.95$, it can be seen that

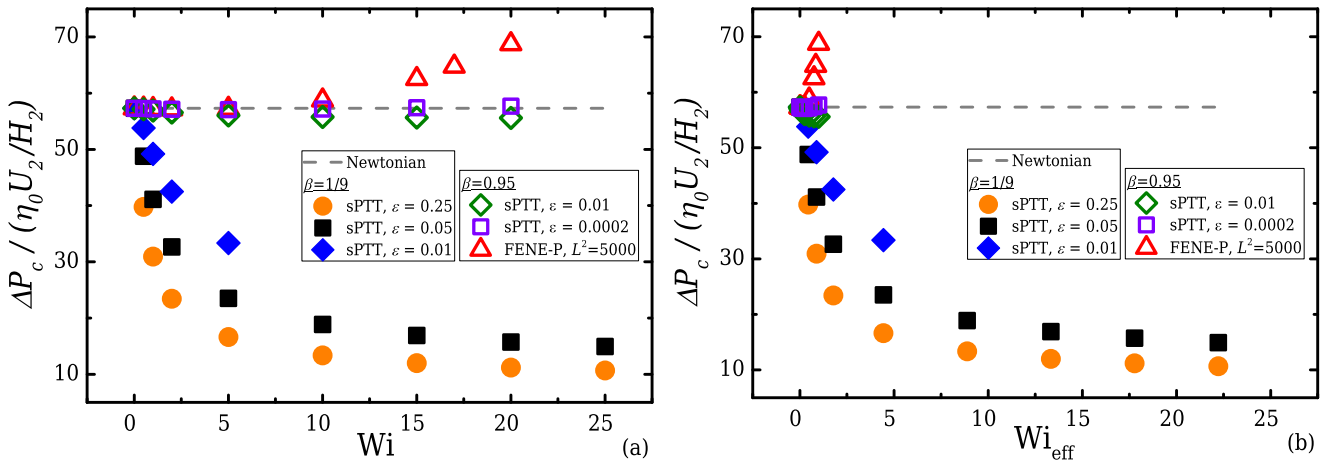

Figure 12: Normalised pressure-drop across the contraction/expansion region for all the investigated cases under creeping-flow conditions for (a) increasing Weissenberg number and (b) as a function of effective Weissenberg numbers. The pressure-drop is evaluated using Eq. (1), following the same procedure used by Ober *et al.* [24].

for the two cases of the sPTT model the Newtonian-like behaviour is once again observed. The evaluated pressure-drop for both cases shows minor deviations from the Newtonian response with increasing Wi and, particularly for the case $\varepsilon = 0.0002$ a very small non-monotonic behaviour is observed, with the evaluated pressure-drop decreasing at small Weissenberg numbers and then gradually increasing as Wi increases. Similar observations have been also reported in Binding *et al.* [66] for a dilute polymer solution described by the Oldroyd-B model with $\beta = 0.9$. On the contrary, for the FENE-P model with $L^2 = 5000$, a small enhancement in pressure-drop is observed for increasing Weissenberg numbers, due to the non-homogeneous flow field (unsteady from a Lagrangian description) and the different responses that are predicted by the models under these conditions (see discussion in Section 3 for Eqs. (11) and (12)). Observations of pressure drop enhancement have also been reported in Nyström *et al.* [70], when employing the constant viscosity FENE-CR model at low extensibility values, with $L^2 = 9, L^2 = 25$ and $L^2 = 100$, for simulating the flow in various axisymmetric contractions. Finally, Fig. 13 shows the evolution of the pressure coefficient $\mathcal{P}$ for all fluids investigated. Ober *et al.* [24] highlighted that this coefficient could serve (i) to verify whether the flow is inertialess ($\mathcal{P} < 1$) or not ($\mathcal{P} > 1$) and (ii) to give a measure of the relative importance of the non-Newtonian effects. Here, since all simulations consider creeping-flow conditions, the parameter $\mathcal{P}$ is, as expected, lower than unity in agreement with Ober *et al.* [24]. Additionally, again in agreement with the experimental study, this coefficient is lower for shear-thinning fluids when compared with the Newtonian fluids. Moreover, it can be seen that for the more concentrated polymer fluids described by the sPTT model with $\varepsilon = 0.25$ and $\varepsilon = 0.05$, the $\mathcal{P}$ coefficient has a non-monotonic behaviour reaching a minimum value for Wi slightly below Wi = 5. Above this Wi value, $\mathcal{P}$ starts to increase, reaching to a plateau for higher Wi. Based on this observation, together with the fact that velocity overshoots for these particular cases start to form when Wi $\gtrsim$ 5, we can infer that from this Weissenberg number, and above, the elastic effects start to be more important than the fluid's shear-thinning characteristics.

4.4. *Flow fields of the e-VROC™*

Figure 14 shows contour-plots of the normalised streamwise velocity at the centreplane, computed under creeping-flow conditions with superimposed streamlines for the more ($\beta = 1/9$) and less ($\beta = 0.95$) concentrated viscoelastic fluids considered. Additionally, the equivalent solution that is obtained for the Newtonian fluid flow is included for comparison (Fig. 14a). For the Newtonian fluid, it can been seen that the flow field is symmetric relative to the middle of the contraction ($x/H_2 = 2$), as expected due to the linear solution of this particular case for creeping-flow conditions. Figure 14b, c and d demonstrate the solution obtained for the viscoelastic fluids with $\beta = 1/9$ described by the sPTT model with $\varepsilon = 0.25$, $\varepsilon = 0.05$ and

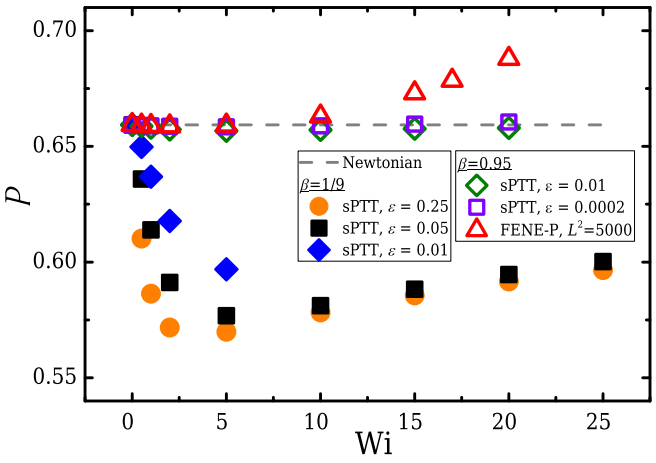

Figure 13: Pressure coefficient $\mathcal{P} = \Delta P_{23}/\Delta P_{14}$ introduced in Ober *et al.* [24] plotted against Weissenberg number.

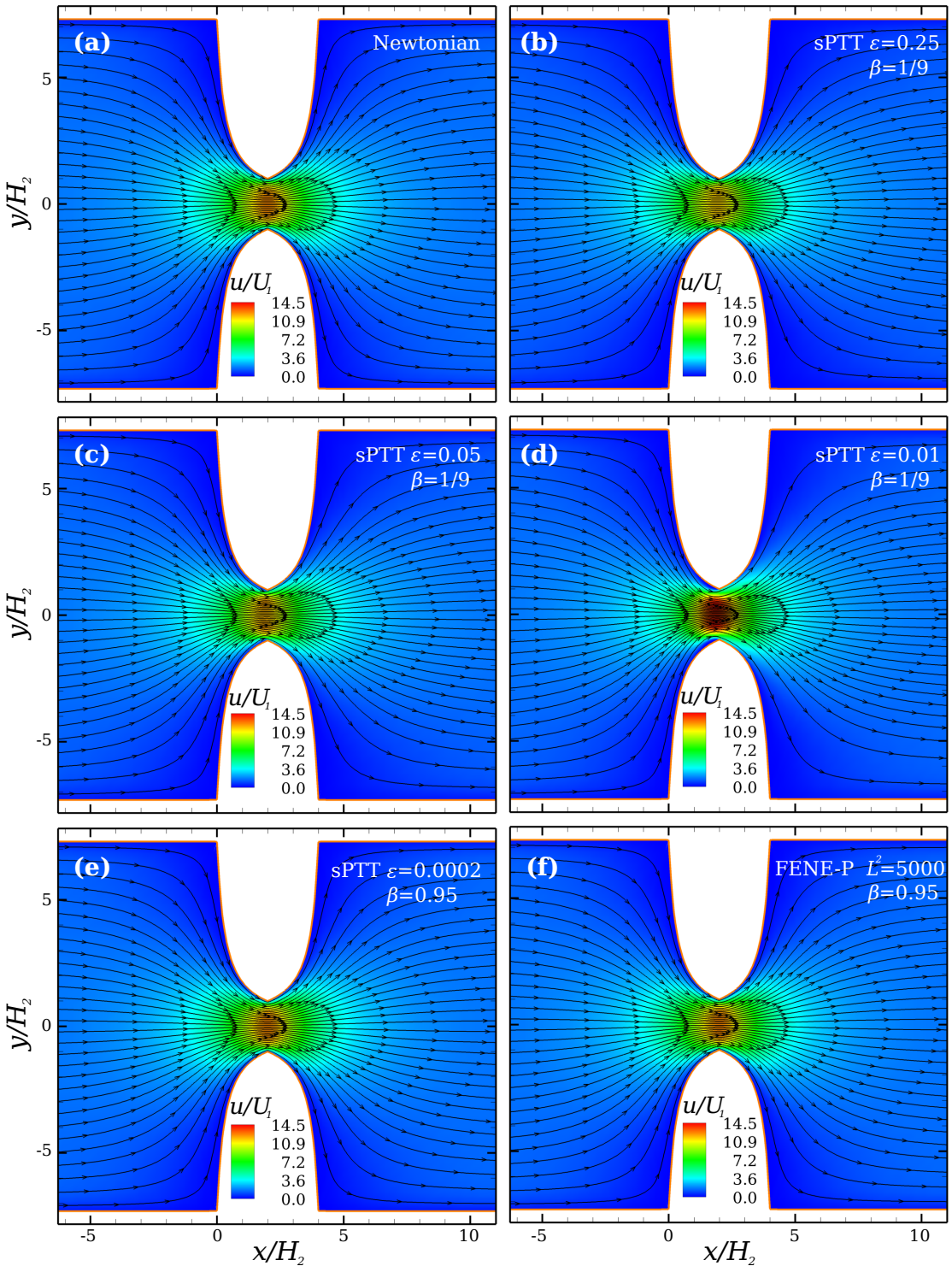

Figure 14: Contour-plots of the normalised streamwise velocity at the flow centreplane with superimposed streamlines at Re $\rightarrow$ 0 for (a) a Newtonian fluid, at Wi = 5.0 for the highly concentrated polymer solutions with β = 1/9 using the sPTT model with (b) ε = 0.25, (c) ε = 0.05, (d) ε = 0.01, and less concentrated polymer solutions with β = 0.95 using the (e) sPTT model with ε = 0.0002 and (f) FENE-P model with L^2 = 5000.

ε = 0.01, respectively, at Wi = 5.0. For the fluids with ε = 0.25 and ε = 0.05, the symmetry of the solution about the constriction is lost, in accordance with the non-symmetric profiles obtained along the flow centreline, (cf. Fig. 8a-d). Finally, for the more elastic fluid, that is the case of ε = 0.01 shown in Fig. 14d, together with the non-symmetric flow field two small lip vortices are formed immediately upstream of the throat of the contraction/expansion. On the contrary for the dilute polymer solutions with β = 0.95 described by the sPTT model with ε = 0.0002 and the FENE-P model with L^2 = 5000, shown

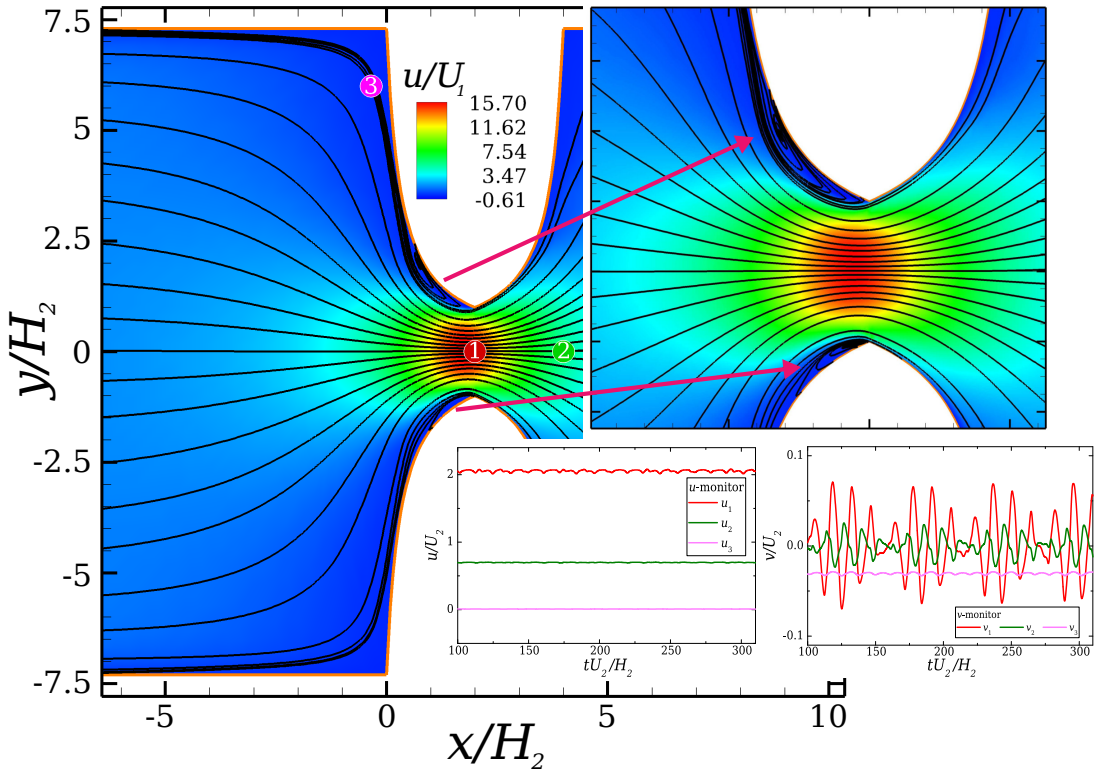

Figure 15: Time snapshot of contours of the normalised streamwise velocity along the flow centreplane at Re $\rightarrow$ 0 with superimposed streamlines for the sPTT fluid with $\varepsilon = 0.01$ at Wi = 10.0. The coloured dots correspond to the employed monitor points of the flow field. The top inset figure is a zoomed view at the throat of the contraction/expansion and shows the small lip vortices that formed at the middle of the contraction/expansion. The bottom insets demonstrate the streamwise $u-$velocity and the lateral v-velocity values obtained at the monitor points.

in Fig. 14e and Fig. 14f respectively, only a slight breaking of symmetry of the velocity field is observed between the two sides of the constriction. This is a consequence of the non-linear terms in the constitutive equations; however, the solution obtained is very similar to the one obtained for the Newtonian fluid, in agreement with previous observations.

For the case of the sPTT model with $\varepsilon = 0.01$ and $\beta = 1/9$, further increases of Weissenberg number result in time-dependent flow. This can be seen in the snapshot of Fig. 15, since the flow is asymmetric with two lip vortices that have different sizes forming immediately upstream of the throat of the contraction/expansion. Moreover, the values obtained for the lateral v-velocity at different locations indicate the periodicity of the flow field with the two vortices increasing and decreasing their intensity over each other along time. For the monitor point #1, the RMS value of the lateral velocity along the flow centreline over a time period is $V_{\mathrm{RMS}}/U_2 = 0.03$, obviously affecting the streamwise velocity which has an RMS deviation from its average value of $U'_{\mathrm{RMS}}/U_2 = 0.02$.

4.5. First normal-stress difference fields of the e-VROC^{TM}

In this section we demonstrate the behaviour of the first normal-stress difference within the e-VROC$^{\mathrm{TM}}$ geometry. The first normal-stress difference is evaluated by taking into account only the polymeric part of the stress tensor and is defined as $N_1 = \tau_{p,11} - \tau_{p,22}$. It is decided to exclude from this definition the solvent contributions, because any anisotropy that occurs in the polymeric first normal-stress difference is directly related to an equivalent anisotropy of the first normal difference of the conformation tensor (see Eq. (9)). Experimentally this can be achieved by flow-induced birefringence measurements [24, 43], an optical method that determines the state of the fluid structure [71]. Ober *et al.* [24] also performed birefringence measurements considering the e-VROC$^{\mathrm{TM}}$ geometry and observed that a strong molecular stretching occurs for the majority of the non-Newtonian fluids investigated.

From the obtained flow field solutions it is straight forward to evaluate N_1 at different flow field planes. By doing that we are able to examine from a different perspective whether the stretching that occurs in the e-VROC$^{\mathrm{TM}}$geometry is due to extensional and/or shear characteristics. Figure 16 shows contour-plots of N_1 at different planes for the case of the sPTT model with $\beta = 1/9$ and $\varepsilon = 0.01$ at Wi = 5. More specifically Figure 16a, b and c illustrate the contour-plots of the normalised N_1 at the flow centreplane, at a distance of $\sim$ 24% and of $\sim$ 82% away from the centreplane, respectively. It can be seen that higher regions of stretching occur closer to the e-VROC$^{\mathrm{TM}}$ walls, indicating that the high values of N_1 are mostly due to shear. Considering now that the experimental birefringence technique used by Ober *et al.* [24] provides average values of the structural anisotropy, Fig. 17d presents the normalised contour-plot of the average value of N_1, evaluated by the corresponding values at different planes. This shows the average is

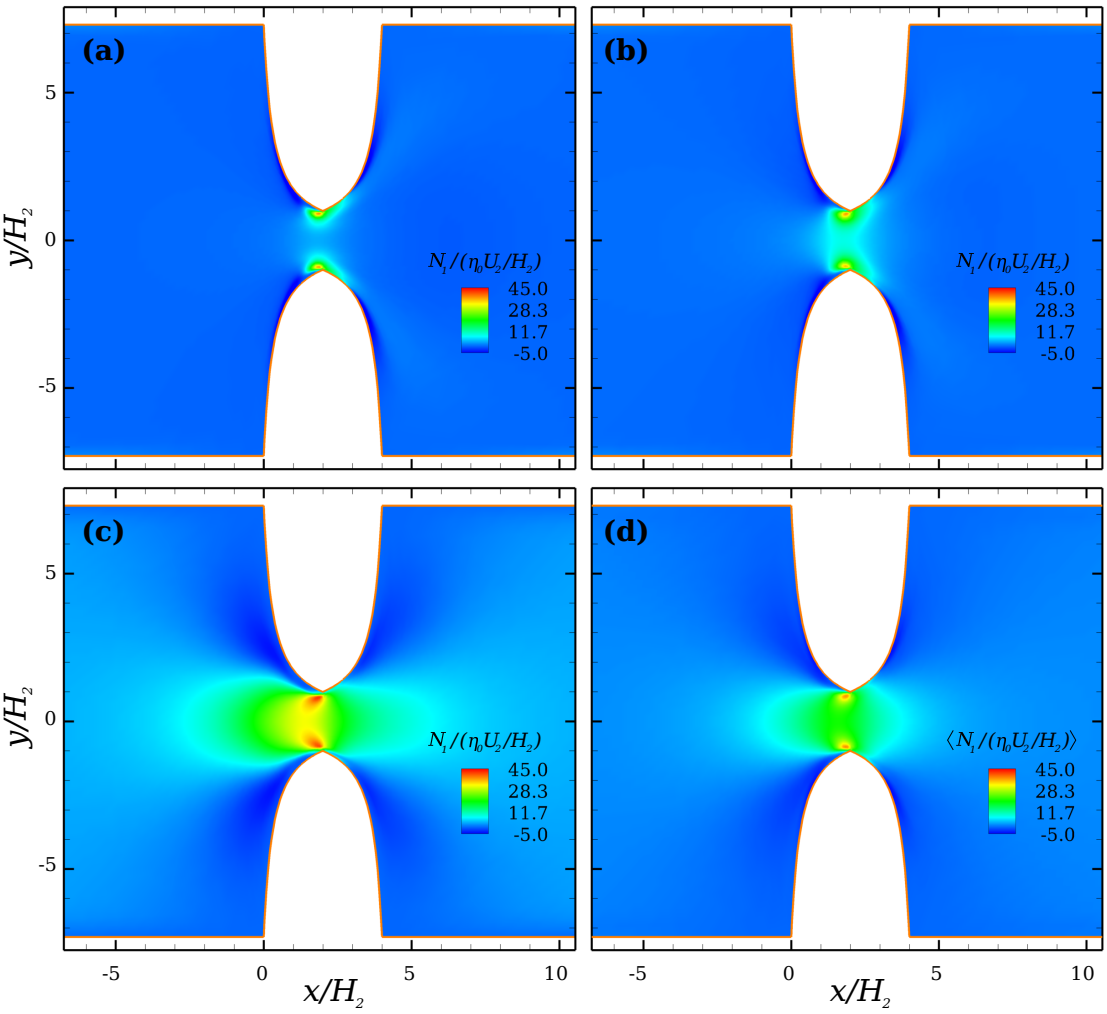

Figure 16: Normalised first normal-stress difference $N_1/(\eta_0 U_2/H_2)$ for the sPTT model with $\beta = 1/9$ and $\varepsilon = 0.01$ at Wi = 5 in the e-VROC^{TM} geometry at different z-planes: (a) centreplane, (b) $\sim 24\%$ away from centreplane, (c) $\sim 82\%$ away from centreplane and (d) average value evaluated by integration on all planes.

mainly determined by the near-wall shear contribution.

The normalised contour-plots of N_1 for the low concentrated polymer solutions ($\beta = 0.95$) produced by the sPTT model with $\varepsilon = 0.0002$ and the FENE-P model with $L^2 = 5000$ are shown in Figs. 17 and 18 respectively. Similar conclusions to the case of concentrated polymer solutions can be read by investigating the behaviour of N_1 at different planes. It can be seen that for both viscoelastic fluid flows, N_1 has low values on the centreplane and also at a distance of $\sim 24\%$ away from the centreplane (cf. Fig. 17a and b for the sPTT with $\varepsilon = 0.0002$; Fig. 18a and b for the FENE-P with $L^2 = 5000$), compared to its equivalent values when flowing closer to the walls (cf. Fig. 17c for the sPTT with $\varepsilon = 0.0002$; Fig. 18c for the FENE-P with $L^2 = 5000$). Therefore, the final average value of N_1 shown in Fig. 17d for the sPTT with $\varepsilon = 0.0002$ and in Fig. 18d for the FENE-P with $L^2 = 5000$, is, as for the previous case of the highly concentrated fluid, mostly influenced by shear-forces rather than strong extension that occurs along or around the centreplane. In Appendix B a discussion regarding the behaviour of the trace of the conformation trace can be found, which provides an alternative way of examining the deformation that occurs in the e-VROC^{TM} geometry.

5. Conclusions

The performance of the e-VROC^{TM} device under creeping-flow conditions for a Newtonian fluid and several shear-thinning viscoelastic fluids was examined, employing full three-dimensional CFD simulations. The relatively high concentrated polymers with $\beta = 1/9$, were described by the sPTT model with $\varepsilon = 0.01$, 0.05 and 0.25, while for the cases of the dilute polymer solutions with $\beta = 0.95$ the sPTT model with $\varepsilon = 0.01$ and $\varepsilon = 0.0002$ and the FENE-P model with $L^2 = 5000$ have been considered. The flow of the Newtonian fluid was simulated as our base flow and illustrated that the geometry is highly affected by shear-effects, displaying only a very narrow region along the flow centreplane that can be considered as extension-dominated. Moreover, the considered length of the constriction is apparently not large enough for the fluid to approach closely the theoretical, well-defined, velocity profile as shown in Nyström *et al.*[70] and discussed in detail in Zografos *et al.* [41], but rather is greatly affected by entrance and exit effects

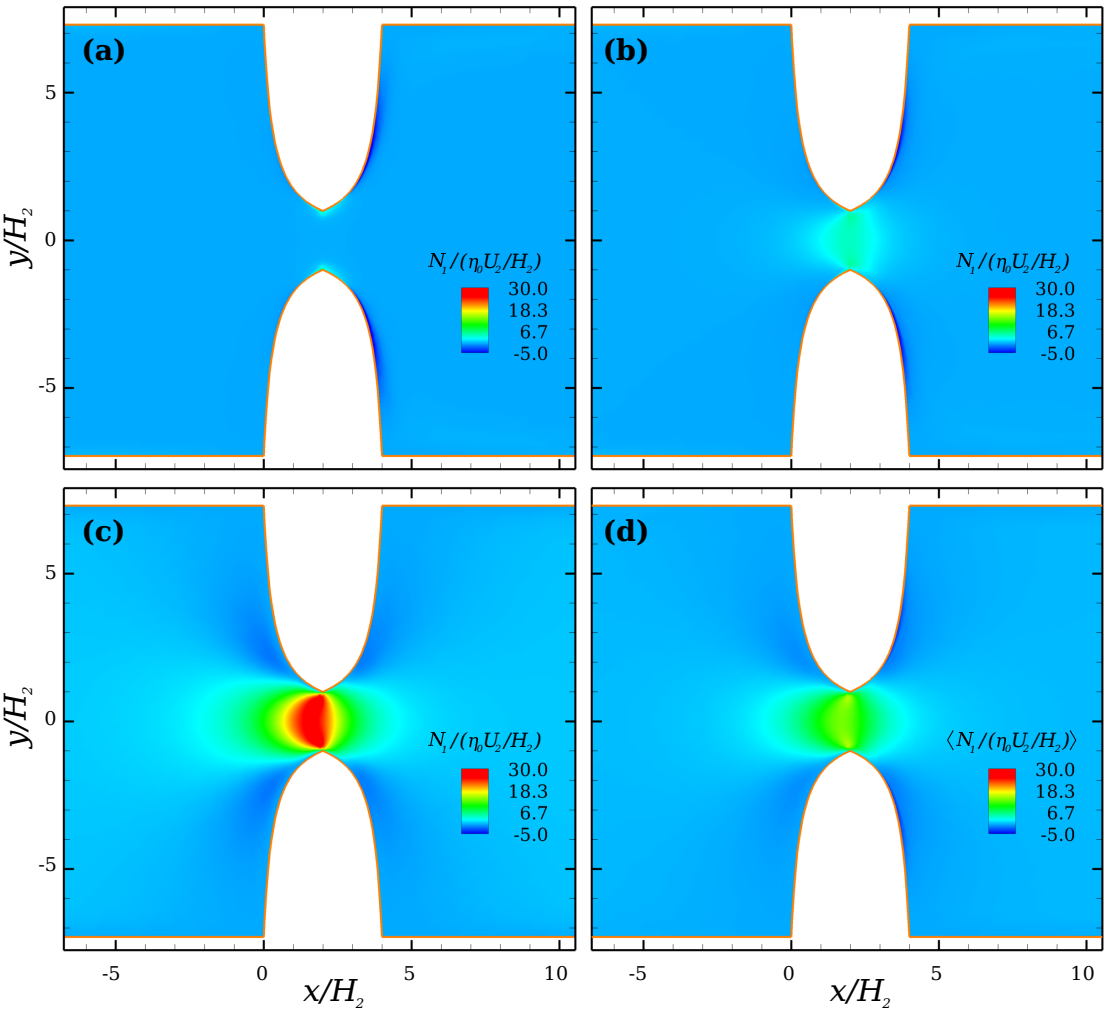

Figure 17: Normalised first normal-stress difference $N_1/(\eta_0 U_2/H_2)$ for the sPTT model with $\beta = 0.95$ and $\varepsilon = 0.0002$ at Wi = 20 in the e-VROC^{TM} geometry at different z-planes: (a) centreplane, (b) $\sim 24\%$ away from centreplane, (c) $\sim 82\%$ away from centreplane and (d) average value evaluated by integration on all planes.

[41]. A non-homogeneous flow is thus generated around the contraction/expansion region, resulting in the generation of a variable strain-rate profile, which is not ideal for an extensional rheometer. To mitigate this problem, one could potentially consider a longer constriction so that the fluid can better manage the entrance, in order to approach an ideal profile. Alternatively, optimisation techniques could be employed in order to create designs that will be more efficient and suitable for a combination of desired contraction/expansion lengths and aspect ratios, which can generate imposed and well-defined flow characteristics [41]. It was shown that the performance of the e-VROC^{TM} geometry is similar to that of a very short abrupt contraction/expansion. It should be mentioned here that for viscoelastic fluids the e-VROC^{TM} configuration is expected to operate more efficiently because of its smoother boundaries compared to the short abrupt geometry, for which it is likely that lip and corner vortices will form at lower Wi.

The use of highly shear-thinning viscoelastic fluids in the e-VROC^{TM} geometry influences the flow kinematics significantly, when compared to a Newtonian fluid. It was shown that for all the cases of the more concentrated shear-thinning polymer solutions the geometry fails to produce a constant strain-rate along the flow centreline even for low Wi, deviating further from the desired behaviour than the Newtonian fluid. This behaviour also affects the pressure-drop along the channel, with all sPTT fluids exhibiting a reduced pressure-drop in comparison to the Newtonian fluid (due to the shear-thinning nature of the sPTT model). As the Weissenberg number increases, velocity overshoots are observed, which also need to be taken into account since they will have an impact on the applied strain rate. On the contrary, for the cases of the dilute polymer solutions ($\beta = 0.95$), it was seen that simulations with the sPTT model resulted in a Newtonian-like behaviour, both in terms of velocity and strain-rate profiles, but also in terms of pressure-drop and first normal-stress difference. When the FENE-P model was employed, a small enhancement in pressure-drop was observed, together with more pronounced velocity overshoots due to the non-homogeneous flow that results in a non-zero value for the extra terms that appear in the constitutive equation in comparison to the sPTT model (cf. Eq. (12)).

Overall, our results show that the e-VROC^{TM} device is able to generate a region of strong extensional flow and may poten-

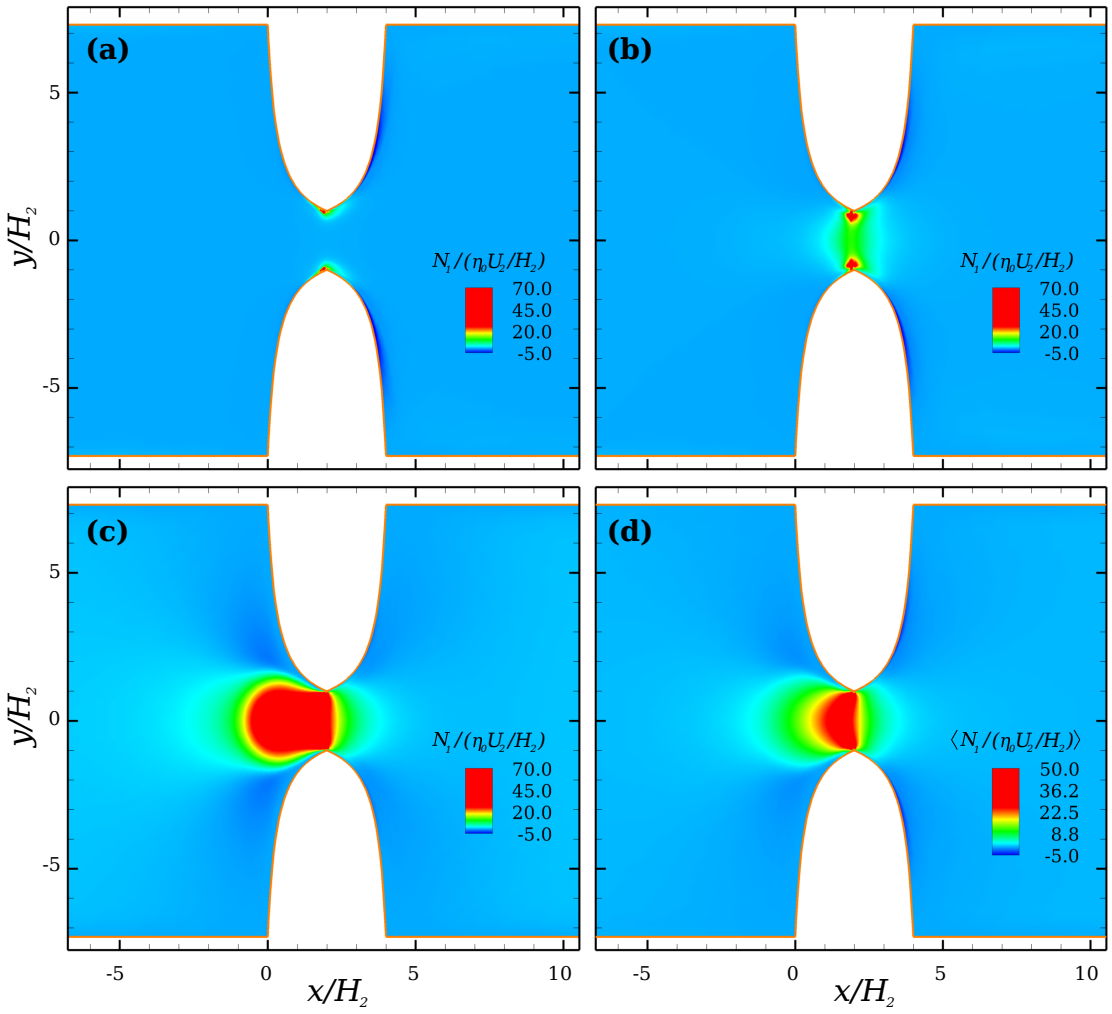

Figure 18: Normalised first normal-stress difference $N_1/(\eta_0 U_2/H_2)$ for the FENE-P model with $\beta = 0.95$ and $L^2 = 5000$ at Wi = 20 in the e-VROC^{TM} geometry at different z-planes: (a) centreplane, (b) $\sim 24\%$ away from centreplane, (c) $\sim 82\%$ away from centreplane and (d) average value evaluated by integration on all planes.

tially be useful for indexing the elasticity of fluids of interest. However, since the actual size of the pure-extension region is found to be small, with the resulting flow field being mainly shear-dominated, care should be taken in the interpretation of the results. This is further supported by the behaviour of N_1, which suggests that the stretching which occurs is mostly due to shear. Further improvements for an extensional rheometer of this type should take into account the shear-thinning characteristics of the fluid samples used. However, it is most likely that these configurations will not operate efficiently simultaneously for both constant viscosity fluids and fluids with shear-dependent viscosity. Moreover, for the most elastic cases considered (both for highly concentrated or dilute solutions), velocity overshoots form along the flow centreline for increasing Weissenberg numbers, an effect that needs to be taken into consideration, especially when one is dealing with samples that are sensitive to large strain-rates.

A. Comparison with experimental results

Here we provide a comparison between the CFD results presented and the experimental study of Ober *et al.* [24] for a Newtonian fluid. It can be seen in Fig. A.19 that upstream of the contraction the experimental profile is in good agreement with the CFD results, capturing well also the transition region where the velocity is much higher from the desired, due to viscous diffusion and possible entrance effects. However, as the fluid advances further from the start of the contraction and flows towards the middle of the constriction, the developed profile generates higher values in the experimental study along the flow centreline. This is due to a scalloping effect that occurs as a consequence of the wet-etching used in the device fabrication, generating boundaries with smooth/rounded vertices [24]. This effect is schematically shown in Fig. A.20 in an attempt to explain these differences. Upstream and downstream of the contraction/expansion and while the aspect ratio is constant and large, the differences due to the scalloping effect do not affect significantly the velocity profile. However, along the length of the constriction where the aspect ratio varies

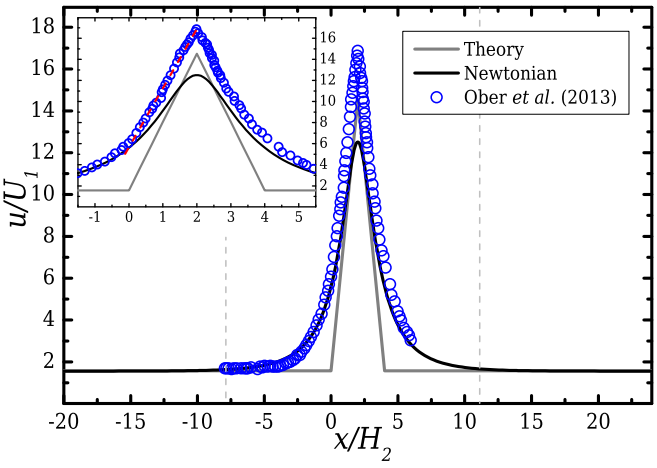

Figure A.19: Normalised streamwise velocity profiles obtained from Ober *et al.* [24] against CFD and theoretical (ideal) profiles discussed in Section 4.1 (see Fig. 1c and d). The vertical *dashed* lines indicate the locations of the pressure sensors P_2 and P_3 placed on the e-VROC^{TM} geometry used by Ober *et al.* [24] (see Fig. 1a), while the theory (ideal) velocity profile is explained in Fig. 1c. The slope of the dashed line in the inset figure corresponds to the actual applied strain-rate.

monotonically, reaching its minimum value at the middle of the contraction/expansion, these design differences influence more significantly the flow field. In reality, the experimental cross-section is smaller compared to the desired (which is not the case for the numerical mesh) and thus the velocities observed experimentally will be higher compared to the theoretical and the CFD velocities, due to mass conservation.

B. Trace of the conformation tensor

In Fig. B.21 a comparison between the contours of the trace of the conformation tensor obtained for low concentration polymer solutions ($\beta = 0.95$) is provided, considering the sPTT model with $\varepsilon = 0.0002$ and the FENE-P model with $L^2 = 5000$. More specifically, Fig. B.21a, c and e correspond to the case of the FENE-P while Fig. B.21b, d and f correspond to the case of the sPTT, with the contours of Tr**A** given at the centreplane, $\sim$ 24% and $\sim$ 82% away from centreplane, respectively. As was seen previously for both cases in Section 4.2, the maximum polymer stretch (expressed now by the trace of the conformation, Tr**A**) clearly occurs closer to the wall and away from the centreplane (at $\sim$ 82% - Fig. B.21e and f). Additionally, for the case of the FENE-P model it can be seen that the maximum extension of the polymer molecule is not reached (i.e. $L^2 = 5000$). Furthermore, it is noticeable that Tr**A** has higher values for the sPTT model compared to the FENE-P model. This may misleadingly lead one to conclude that the stresses in the sPTT model are correspondingly higher but the opposite behaviour is, in fact, observed as was shown in Figs. 17 and 18.

To explain the behaviour observed, Eq. (9) is rearranged for both models and solved for the trace of the conformation:

$$\mathrm{Tr}\mathbf{A} = \begin{cases} \frac{\lambda}{\eta_p}\left({\tau_{xx}}^p + {\tau_{yy}}^p + {\tau_{zz}}^p\right) + 3, & \text{sPTT} \\ \left[\frac{\lambda}{\eta_p}\left({\tau_{xx}}^p + {\tau_{yy}}^p + {\tau_{zz}}^p\right) + 3a\right]{f_F}^{-1}, & \text{FENE-P} \end{cases} \tag{B.1}$$

where it is reminded that $f_F = 1 + [3a + (\lambda/\eta_p)\mathrm{Tr}\boldsymbol{\tau}_p]/L^2$, as discussed in Section 3. From the above definitions it can be seen that this difference occurs due to the presence of the f_F term ($a \simeq 1$) which is greater than unity. Thus care has to be taken when comparing the Tr**A** levels between different models.

Acknowledgements

K. Z. and R. J. P. acknowledge funding from the EPSRC (UK) through Grant No. EP/M025187/1.

References

[1] S. J. Haward, Microfluidic extensional rheometry using stagnation point flow, Biomicrofluidics 10 (043401)(2016) . doi:10.1063/1.4945604.

[2] F. A. Morrison, An introduction to fluid mechanics, Cambridge University Press, New York, 2013.

[3] H. A. Barnes, Handbook of Elementary Rheology, University of Wales Institute of Non-Newtonian Fluid Mechanics, 2000.

[4] M. S. N. Oliveira, M. A. Alves, F. T. Pinho, Microfluidic Flows of Viscoelastic Fluids, Wiley-V C H Verlag GMBH, 2012, Ch. 6, pp. 131–174. doi:10.1002/9783527639748.ch6.

[5] S. Varchanis, Y. Dimakopoulos, C. Wagner, J. Tsamopoulos, How viscoelastic is human blood plasma?, Soft Matter 14 (2018) 4238–4251. doi:10.1039/c8sm00061a.

[6] D. Pinho, T. Yaginuma, R. Lima, A microfluidic device for partial cell separation and deformability assessment, Biochip. J. 7 (2013) 367–374. doi:10.1007/s13206-013-7408-0.

[7] T. Yaginuma, M. S. N. Oliveira, R. Lima, T. Ishikawa, T. Yamaguchi, Human red blood cell behavior under homogeneous extensional flow in a hyperbolic-shaped microchannel, Biomicrofluidics 7 (054110)(2013) . doi:10.1063/1.4820414.

[8] H. A. Barnes, J. F. Hutton, K. Walters, An introduction to rheology, Elsevier, Amsterdam, 1989.

[9] P. Fischer, E. J. Windhab, Rheology of food materials, Curr. Opin. Colloid InterfaceSci. 16 (2011) 36–40. doi:10.1016/j.cocis.2010.07.003.

[10] P. C. Sousa, F. T. Pinho, M. A. Alves, M. S. N. Oliveira, A review of hemorheology: Measuring techniques and recent advances, Korea-Aust. Rheol. J. 28 (2016) 1–22. doi:10.1007/s13367-016-0001-z.

[11] E. K. Sackmann, A. L. Fulton, D. J. Beebe, The present and future role of microfluidics in biomedical research, Nature 507 (2014) 181–189.

[12] C. J. Pipe, G. H. McKinley, Microfluidic rheometry, Mech. Res. Commun. 36 (2009) 110–120. doi:10.1016/j.mechrescom.2008.08.009.

[13] F. J. Galindo-Rosales, M. S. N. Oliveira, M. A. Alves, Microdevices for extensional rheometry of low viscosity elastic liquids: a review, Microfluid Nanofluid 14 (2013) 1–19. doi:10.1007/s10404-012-1028-1.

[14] D. V. Boger, Circular entry flows of inelastic and viscoelastic fluids., In: Mujumdar A. S. , Mashelkar R. A. (eds) Advances of transport processes, vol 2. Wiley Eastern, New Delhi (1987) 43–98.

[15] J. P. Rothstein, G. H. McKinley, The axisymmetric contraction-expansion: The role of extensional rheology on vortex growth dynamics and the enhanced pressure drop, J. Non-Newton. Fluid Mech. 98 (2001) 33–63. doi:10.1016/S0377-0257(01)00094-5.

[16] L. E. Rodd, T. P. Scott, D. V. Boger, J. J. Cooper-White, G. H. McKinley, The inertio-elastic planar entry flow of low-viscosity elastic fluids in micro-fabricated geometries, J. Non-Newton. Fluid Mech. 129 (2005) 1–22. doi:10.1016/j.jnnfm.2005.04.006.

[17] L. E. Rodd, J. J. Cooper-White, D. V. Boger, G. H. McKinley, Role of the elasticity number in the entry flow of dilute polymer solutions in micro-fabricated contraction geometries, J. Non-Newton. Fluid Mech. 143 (2007) 170–191. doi:10.1016/j.jnnfm.2007.02.006.

[18] M. S. N. Oliveira, M. A. Alves, F. T. Pinho, G. H. McKinley, Viscous flow through microfabricated hyperbolic contractions, Exp. Fluids 43 (2007) 437–451. doi:10.1007/s00348-007-0306-2.

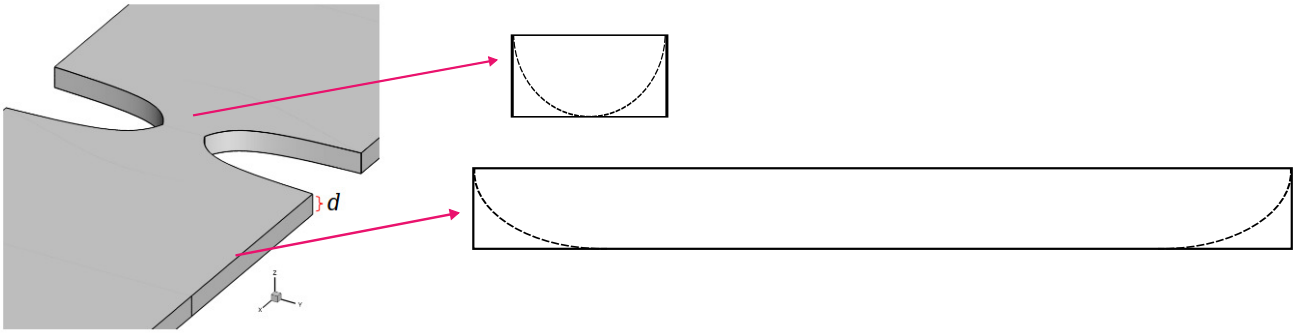

Figure A.20: Scalloping effect shown schematically for the cross-section downstream and at the middle of the contraction/expansion.

[19] O. Hassager, Working group on numerical techniques (Vth Workshop on Numerical Methods in Non-Newtonian Flow), J. Non-Newton. Fluid Mech. 29 (1988) 2–5.

[20] R. G. Owens, T. N. Phillips, Computational Rheology, Imperial College Press, 2002.

[21] P. J. Oliveira, Asymmetric flows of viscoelastic fluids in symmetric planar expansion geometries, J. Non-Newton. Fluid Mech. 114 (2003) 33–63. doi:10.1016/S0377-0257(03)00117-4.

[22] M. A. Alves, P. J. Oliveira, F. T. Pinho, Benchmark solutions for the flow of Oldroyd-B and PTT fluids in planar contractions, J. Non-Newton. Fluid Mech. 110 (2003) 45–75. doi:10.1016/S0377-0257(02)00191-X.

[23] M. S. N. Oliveira, L. E. Rodd, G. H. McKinley, M. A. Alves, Simulations of extensional flow in microrheometric devices, Microfluid Nanofluid 5 (2008) 809–826. doi:10.1007/s10404-008-0277-5.

[24] T. J. Ober, S. J. Haward, C. J. Pipe, J. Soulages, G. H. McKinley, Microfluidic extensional rheometry using a hyperbolic contraction geometry, Rheol Acta 52 (2013) 529–546. doi:10.1007/s00397-013-0701-y.

[25] M. A. Alves, P. J. Oliveira, F. T. Pinho, On the effect of contraction ratio in viscoelastic flow through abrupt contractions, J. Non-Newton. Fluid Mech. 122 (2004) 117–30. doi:10.1016/j.jnnfm.2004.01.022.

[26] M. A. Alves, R. J. Poole, Divergent flow in contractions, J. Non-Newton. Fluid Mech. 144 (2007) 140–148. doi:10.1016/j.jnnfm.2007.04.003.

[27] G. H. McKinley, L. E. Rodd, M. S. N. Oliveira, J. J. Cooper-White, Extensional flows of polymer solutions in microfluidic converging/diverging geometries, J. Cent. South Univ. Technol. 14 (2007) 6–9. doi:10.1007/s11771-007-0202-1.

[28] M. S. N. Oliveira, P. J. Oliveira, F. T. Pinho, M. A. Alves, Effect of contraction ratio upon viscoelastic flow in contractions: The axisymmetric case, J. Non-Newton. Fluid Mech. 147 (2007) 92–108. doi:10.1016/j.jnnfm.2007.07.009.

[29] R. J. Poole, F. T. Pinho, M. A. Alves, P. J. Oliveira, The effect of expansion ratio for creeping expansion flows of UCM fluids, J. Non-Newton. Fluid Mech. 163 (2009) 35–44. doi:10.1016/j.jnnfm.2009.06.004.

[30] F. N. Cogswell, Converging flow and stretching flow: a compilation, J. Non-Newton. Fluid Mech. 4 (1978) 23–38. doi:10.1016/0377-0257(78)85004-6.

[31] D. F. James, G. M. Chandler, S. J. Armour, A converging channel rheometer for the measurment of extensional viscosity, J. Non-Newton. Fluid Mech. 35 (1990) 421–443. doi:10.1016/0377-0257(90)85063-5.

[32] F. N. Cogswell, Measuring the extensional rheology of polymer melts, Trans. Soc. Rheol. 16 (1972) 383–403. doi:10.1122/1.549257.

[33] B. Keshavarz, G. H. McKinley, Micro-scale extensional rheometry using hyperbolic converging/diverging channels and jet breakup, Biomicrofluidics 10 (043502)(2016) . doi:10.1063/1.4948235.

[34] L. Campo-Deaño, F. J. Galindo-Rosales, F. T. Pinho, M. A. Alves, M. S. N. Oliveira, Flow of low viscosity Boger fluids through a microfluidic hyperbolic contraction, J. Non-Newton. Fluid Mech. 166 (2011) 1286–1296. doi:10.1016/j.jnnfm.2011.08.006.

[35] P. C. Sousa, F. T. Pinho, M. S. N. Oliveira, M. A. Alves, Extensional flow of blood analog solutions in microfluidic devices, Biomicrofluidics 5 (014108)(2011) . doi:10.1063/1.3567888.

[36] R. O. Rodrigues, D. Pinho, V. Faustino, R. Lima, A simple microfluidic device for the deformability assessment of blood cells in a continuous flow, Biomed. Microdevices 17 (108)(2015) . doi:10.1007/s10544-015-0014-2.

[37] S. S. Lee, Y. Yim, K. H. Ahn, S. J. Lee, Extensional flow-based assesment of red blood cell deformability using a hyperbolic converging microchannel, Biomed. Microdevices 11 (2009) 1021–1027. doi:10.1007/s10544-009-9319-3.

[38] T. Wu, J. J. Feng, Simulation of malaria-infected red blood cells in microfluidic channels: Passage and blockage, Biomicrofluidics 7 (044115)(2013) . doi:10.1063/1.4817959.

[39] H. Zolfaghari, D. Izbassarov, M. Muradoglu, Simulations of viscoelastic two-phase flows in complex geometries, Comput. Fluids 156 (2017) 548–561. doi:10.1016/j.compfluid.2017.05.026.

[40] E. Kadivar, Modeling droplet deformation through convergingdiverging microchannels at low reynolds number, Acta Mech 229 (2018) 4239–4250. doi:10.1007/s00707-018-2225-0.

[41] K. Zografos, F. Pimenta, M. A. Alves, M. S. N. Oliveira, Microfluidic converging/diverging channels optimised for homogeneous extensional deformation, Biomicrofluidics 10 (043508)(2016) . doi:10.1063/1.4954814.

[42] H. S. Lee, S. Muller, A differential pressure extensional rheometer on a chip with fully developed elongational flow, J. Rheol. 61 (2017) 1049–1059. doi:10.1122/1.4998175.

[43] S. J. Haward, M. S. N. Oliveira, M. A. Alves, G. H. McKinley, Optimized cross-slot geometry for microfluidic extensional rheometry, Phys. Rev. Lett. 109 (2012) 128301. doi:10.1103/PhysRevLett.109.128301.

[44] D. V. Boger, A highly elastic constant-viscosity fluid, J. Non-Newton. Fluid Mech. 3 (1977/1978) 87–91. doi:10.1016/0377-0257(77)80014-1.

[45] N. Phan-Thien, R. I. Tanner, A new constitutive equation derived from network theory, J. Non-Newton. Fluid Mech. 2 (1977) 353–365. doi:10.1016/0377-0257(77)80021-9.

[46] R. B. Bird, P. J. Dotson, N. L. Johnson, Polymer solution rheology based on a finitely extensible bead-spring chain model, J. Non-Newton. Fluid Mech. 7 (1980) 213–235. doi:10.1016/0377-0257(80)85007-5.

[47] P. J. Oliveira, An exact solution for tube and slit flow of a fene-p fluid, Acta Mech. 158 (2002) 157–167. doi:10.1007/BF01176906.

[48] A. Afonso, P. J. Oliveira, F. T. Pinho, M. A. Alves, The log-conformation tensor approach in the finite-volume method framework, J. Non-Newtonian Fluid Mech. 157 (2009) 55–65. doi:10.1016/j.jnnfm.2008.09.007.

[49] P. J. Oliveira, F. T. Pinho, Analytical solution for fully developed channel and pipe flow of Phan-Thien-Tanner fluids, J. Fluid. Mech. 387 (1999) 271–280. doi:10.1017/S002211209900453X.

[50] M. A. Alves, F. T. Pinho, P. J. Oliveira, Study of steady pipe and channel flows of a single-mode Phan-Thien-Tanner fluid, J. Non-Newton. Fluid Mech. 101 (2001) 55–76. doi:10.1016/S0377-0257(01)00159-8.

[51] R. B. Bird, R. C. Armstrong, O. Hassager, Dynamics of polymeric liquids. Volume 1: Fluid Dynamics, John Wiley & Sons, New York, 1987.

[52] P. J. Oliveira, Alternative derivation of differential constitutive equations of the oldroyd-b type, J. Non-Newton. Fluid Mech. 160 (2009) 40–46. doi:10.1016/j.jnnfm.2008.11.013.

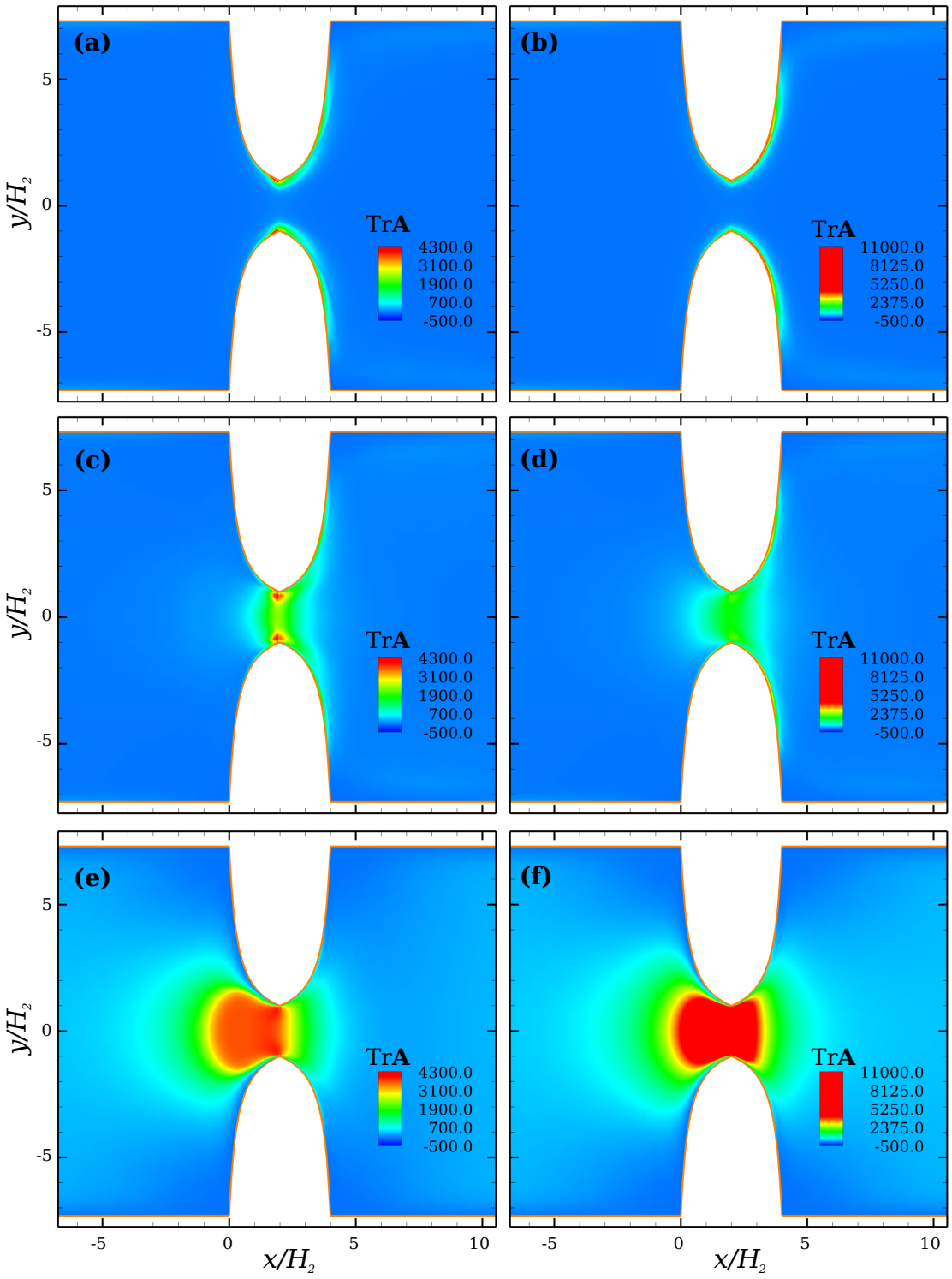

Figure B.21: Contour-plots of the trace of the conformation tensor for the FENE-P model with $\beta = 0.95$ and $L^2 = 5000$ (a, c, e) and the sPTT model with $\beta = 0.95$ and $\varepsilon = 0.0002$ (b, d, f) at Wi = 20 in the e-VROC^{TM} geometry at different z-planes: (a,b) centreplane, (c,d) $\sim 24\%$ away from centreplane, (e,f) $\sim 82\%$ away from centreplane.

[53] R. J. Poole, M. Davoodi, K. Zografos, On the similarities between the simplified Phan-Thien Tanner (sPTT) and FENE-P models, The British Society of Rheology, Rheology Bulletin (29-34)(2019) .
URL https://livrepository.liverpool.ac.uk/3056719/

[54] P. J. Oliveira, F. T. Pinho, G. A. Pinto, Numerical simulation of non-linear elastic flows with a general collocated finite-volume method, J. Non-Newton. Fluid Mech. 79 (1998) 1–43. doi:10.1016/S0377-0257(98)00082-2.

[55] P. J. Oliveira, On the numerical implentation of nonlinear viscoelastic models in a finite-volume method, Numer Heat Transf. 40 (2001) 283–301. doi:10.1080/104077901317091695.

[56] R. Fattal, R. Kupferman, Constitutive laws for the matrix-logarithm of the

conformation tensor, J. Non-Newton. Fluid Mech. 123 (2004) 281–285. doi:10.1016/j.jnnfm.2004.08.008.

[57] A. M. Afonso, P. J. Oliveira, F. T. Pinho, M. A. Alves, Dynamics of high Deborah number entry flows: a numerical study, J. Fluid. Mech. 677 (2011) 272–304. doi:10.1017/jfm.2011.84.

[58] C. M. Rhie, W. L. Chow, Numerical study of the turbulent flow past an airfoil with trailing edge separation., AIAA J. 21 (1983) 1525–1532. doi:10.2514/3.8284.

[59] M. A. Alves, P. J. Oliveira, F. T. Pinho, A convergent and universally bounded interpolation scheme for the treatment of advection, Int. J. Numer. Meth. Fluids 41 (2003) 47–75. doi:10.1002/fld.428.

[60] J. S. Lee, R. Dylla-Spears, N. P. Teclemariam, S. J. Muller, Microfluidic four-roll mill for all flow types, Appl. Phys. Lett. 90 (074103)(2007) . doi:10.1063/1.2472528.

[61] G. G. Fuller, L. G. Leal, Flow birefringence of dilute polymer solutions in two-dimensional flows, Rheol. Acta 19 (1980) 580–600. doi:10.1007/BF01517512.

[62] F. M. White, Viscous Fluid Flow, 3rd Edition, McGraw-Hill, 2006.

[63] N. Burshtein, K. Zografos, A. Q. Shen, R. J. Poole, S. J. Haward, Inertioelastic flow instability at a stagnation point, Phys. Rev. X 7 (041039)(2017) . doi:10.1103/PhysRevX.7.041039.

[64] K. Zografos, N. Burshtein, A. Q. Shen, S. J. Haward, R. Poole, Elastic modifications of an inertial instability in a 3d cross-slot, J. Non-Newton. Fluid Mech. 262 (2018) 12–24. doi:10.1016/j.jnnfm.2018.02.002.

[65] A. Afonso, F. T. Pinho, Numerical investigation of the velocity overshoots in the flow of viscoelastic fluids inside a smooth contraction, J. Non-Newton. Fluid Mech. 139 (2006) 1–20. doi:10.1016/j.jnnfm.2006.05.012.

[66] D. M. Binding, P. M. Phillips, T. N. Phillips, Contraction/expansion flows: The pressure drop and related issues, J. Non-Newton. Fluid Mech. 137 (2006) 31–38. doi:10.1016/j.jnnfm.2006.03.006.

[67] R. J. Poole, M. A. Alves, P. J. Oliveira, F. T. Pinho, Plane sudden expansion flows of viscoelastic liquids, J. Non-Newton. Fluid Mech. 146 (2007) 79–91. doi:10.1016/j.jnnfm.2006.11.001.

[68] P. C. Sousa, P. M. Coelho, M. S. N. Oliveira, M. A. Alves, Three-dimensional flow of Newtonian and Boger fluids in squaresquare contractions, J. Non-Newton. Fluid Mech. 160 (2009) 122–139. doi:10.1016/j.jnnfm.2009.03.009.

[69] S. Nigen, K. Walters, Viscoelastic contraction flows: comparison of axisymmetric and planar configuration, J. Non-Newton. Fluid Mech. 102 (2002) 343–359. doi:10.1016/S0377-0257(01)00186-0.

[70] M. Nyström, H. R. T. Jahromi, M. Stading, M. F. Webster, Numerical simulations of Boger fluids through different contraction configurations for the development of a measuring sytem for extensional viscosity, Rheol Acta 51 (2012) 713–727. doi:10.1007/s00397-012-0631-0.

[71] G. G. Fuller, Optical rheometry, Annu. Rev. Fluid Mech. 22 (1990) 387–417. doi:10.1146/annurev.fl.22.010190.002131.